Post-Spinel and Cobalt Phosphate Frameworks as Cathode Materials for Sodium-ion Batteries

A thesis submitted in Partial Fulfilment of the Degree of

MASTER OF SCIENCE

as a part of

Integrated Ph.D. Programme (Chemical Science)

By

Aditi Chiring

New Chemistry Unit
Jawaharlal Nehru Centre for Advanced Scientific Research
(*A deemed University*)
Bangalore, India
(March 2019)

Dedicated to my beloved family ...

DECLARATION

I hereby declare that the matter embodied in this thesis entitled "*Post-Spinel and Cobalt Phosphate Frameworks as Cathode Materials for Sodium-ion Batteries*" is the result of investigations carried out by me at Energy Storage and Conversion Laboratory, New Chemistry Unit, Jawaharlal Nehru Centre for Advanced Scientific Research, Bengaluru, India under the supervision of Dr. Premkumar Senguttuvan. This work has not been submitted elsewhere for the award of any degree or diploma.

In keeping with the general practice in reporting scientific observations, due acknowledgement has been made whenever the work described is based on the findings of other investigators. Any omission that might have occurred by oversight or error of judgement is regretted.

Date:

Bengaluru, India Aditi Chiring

CERTIFICATE

I hereby declare that the matter in the thesis entitled "*Post-Spinel and Cobalt Phosphate Frameworks as Cathode Materials for Sodium-ion Batteries*" has been carried out by Ms. Aditi Chiring at New Chemistry Unit, Jawaharlal Nehru Centre for Advanced Scientific Research, Bengaluru, India under my supervision and that it has not been submitted elsewhere for the award of any degree or diploma.

Date: Dr. Premkumar Senguttuvan

Bengaluru, India (Research Supervisor)

ACKNOWLEDGMENTS

First and foremost, I would like to thank my research supervisor, Dr. Premkumar Senguttuvan, for giving me an opportunity to work under his guidance. I thank him for introducing me to the interesting area of sodium-ion batteries, suggesting me a research problem and guiding me throughout. I greatly admire his enthusiasm towards science and life. I shall remain ever indebted to him for bearing with me throughout the course of this work. Without his support and encouragement, this thesis would not have been possible.

I would like to thank Prof. C. N. R. Rao, FRS, the chairman of New Chemistry Unit (NCU) for his generous support and encouragement throughout my stay in JNCASR. His enthusiasm, dedication and relentless pursuit of science are truly motivating and propelling. His presence has given me immense inspiration to indulge in active research. I also thank him for providing the infrastructure and facilities to carry out my research work.

I thank my collaborators Prof. Swapan K Pati, and Ms. Madhulika Mazumdar for their fruitful scientific collaborations and all their insightful discussions.

I am thankful to all my labmates and summer interns: Mr. Subham Ghosh, Ms. Vinita Ahuja, Dr. Nabadyuti Barman, Mr. Utsav Dey, Mr. Nirmal, Mr. Rishikesh, Ms. Aswathi and Ms Tristha for their fruitful discussions and cheerful company. I especially thank Mr. Subham for aiding me in many projects.

I thank my course work instructors: Prof. S. J. George, Prof. R. Viswanatha, Prof. J. Haldar, Prof. K. Biswas, Prof. S. C. Peter, Prof. H. Ila, Dr. S. Agasti, Dr. Premkumar, Prof. S. Balasubramanian, Prof. A. Sundersan, Prof. Eswaramoorthy, Prof. S. Rajaram, Prof. T. K. Maji, Prof. S. Sampath (IISc) and Dr. Chinmoy Ranjan (IISc) for their excellent course work.

I would like to express my sincere thanks to Prof. S. C. Peter for providing me the space and resources to work in his lab for the initial two months of my M.S work. I extend the thanks to all the people from his lab for being so welcoming.

I thank all the Teacher's Assistants for their help, valuable discussions and introduction to the way of research.

I am thankful to the technical staff Ms. Selvi, Mrs. T. Usha, Mr. Vasu and Mr. Anil for help in measurements. I extend my thanks to Mr. Naveen, Mrs. Ramya, Ms. Shweta, Ms. Melissa and all the academic, administrative, security, complab, hostel and Dhanvantri staff for their help in making our life easier.

I am thankful to JNCASR for financial support and fellowship.

My sincere thanks to all my 2016 Integrated. PhD batchmates for making my life memorable and comfortable here at JNC. My special thanks to Amit, Sushmita, Ekashmi, and Swaraj for always being there for me; Ankur and Debashish for giving me a break to the outside world when I need one; Asmita, Avinav, Sayan and Yash for their constant words of encouragement.

I express my gratitude to all my school and undergraduate teachers, who have taught me the value of education and life itself.

I thank all my juniors and seniors, whose list of names is too long, but who, nevertheless, have inspired me at some moment through personal interactions.

Finally, and most importantly, I am grateful to my family, especially my parents, Himen Kumar Chiring and Kusum Chiring and sister Bhaswati for their love, support, belief and constant encouragement throughout my life.

PREFACE

In search for cleaner sources of energy production, there also arises a need for better energy storage and conversion systems. Rechargeable batteries are an ideal choice as they have high round trip efficiency and acceptable values of energy densities for application in portable electronics and electric vehicles. Lithium-ion Batteries (LIBs) have currently captured this market. However, due to the high cost of lithium precursors, LIBs have not been mass produced for grid energy storage. Sodium-ion Batteries (SIBs) are appealing from this view point because of the abundance of raw materials and similarity of sodium with lithium chemistry. It is yet to achieve the operating cell voltages and capacities corresponding to commercial LIBs. This is mostly limited by the electrode potential (vs Na^{+}/Na^{0}) and capacities of the cathode materials. Thus, there is a constant challenge is to obtain cathode materials with a higher energy densities. This thesis entitled "*Post-Spinel and Cobalt Phosphate Frameworks as Cathode Materials for Sodium-ion Batteries*" contains results of investigations carried out on two classes of cathode materials for SIBs. It is divided into three chapters.

Chapter 1 Introduction to Sodium-ion Batteries: Herein, I have tried to cover a brief outlay of the concepts and terms used in SIBs. I have also tried to include a few of the promising cathode materials.

Chapter 2 High Voltage $NaCoPO_4$ Cathodes for Rechargeable Sodium-ion Batteries: The use of polyanionic compounds as cathode materials over their corresponding oxides is attractive as they generally have greater structural and chemical stability, higher potential for a given $M^{n+/(n+1)+}$ redox couple and possesses rich structural diversity. Olivine $LiFePO_4$ is one such

compound that has been extensively studied in batteries since its discovery in 1997 by Goodenough *et al*. However, attempts to prepare its sodium analogous olivine structure for $NaMPO_4$ (M= Fe, Mn) has been elusive via conventional methods and resulted in the formation of the thermodynamically favored but electrochemically inactive maricite structure. Here we report the formation of different polymorphs of $NaCoPO_4$ from two sets of precursors, studied using *in-situ* temperature dependent XRD. Our studies show that the previously reported high temperature β-$NaCoPO_4$ can be formed at a much lower temperature (i.e. at ~350 ^oC) and the higher temperature phase (γ-$NaCoPO_4$) is actually a novel polymorph with Co^{2+} in penta-coordinated environment. On rapid cooling, this polymorph transforms to the known β-$NaCoPO_4$ polymorph.

Chapter 3 Chemical Pressure-Stabilized Post Spinel-$NaMnSnO_4$ Cathode for SIBs: Spinel $LiMn_2O_4$ is a popular cathode material for LIBs. Synthesizing analogous $NaMn_2O_4$ in the spinel structure is challenging due to thermodynamic stability of the compound. However, post-spinel $NaMn_2O_4$ (named as such because the compounds were initially achieved by subjecting a spinel phase to high pressure) could be synthesized at a high temperature and pressure (1373 K and 4.5 GPa respectively) and is found to be stable at ambient conditions. In this work, we have made an attempt to induce chemical pressure within the system by use of a heavy cation, i.e. Sn^{4+} in the framework to synthesize $NaFeSnO_4$ and $NaMnSnO_4$. We have attempted to characterize the as-prepared samples with scanning electron microscopy (SEM), X-ray Diffraction (XRD) and GCPL measurements.

TABLE OF CONTENTS

Chapter 1

Introduction to Sodium-ion Batteries

1.1 Introduction

The industrial revolution from the mid-1700s to the mid-1800s brought about a major change in the standard of living for the general population. There was a rapid development in the fields of chemical manufacturing, automobile engineering and textile factories. However, it came at a cost to the environment and public health. As these industries were heavily dependent on fossil-fuel based energy (coal, natural gas, oil), it led to emission of greenhouse gases like CO_2 as well as particulate matter leading to dense fogs and air pollution. Fossil-fuel based energy accounts to 70% of the World Energy Consumption in 2015, which is responsible for about 32 Gt of CO_2 emissions.[1] This situation is even more pertinent in a country like India, which has nine of the top ten most polluted cities in the world in terms of particulate matter concentration.[2] Thus, the need of the hour is research on alternative sources of green energy. The challenge is not only the production of energy from renewable sources like solar and wind but also the storage and transportation of it. Electrical energy storage in the form of capacitors, batteries and fuel cells can partially solve such problem. Figure 1.1 shows a projected scenario from the World Energy Outlook 2015, where a future with electrical energy, sans fossil-fuels, will lead us closer to CO_2 emissions for Sustainable Development than the current and planned policies (New Policies Scenario) will by 2040.[1]

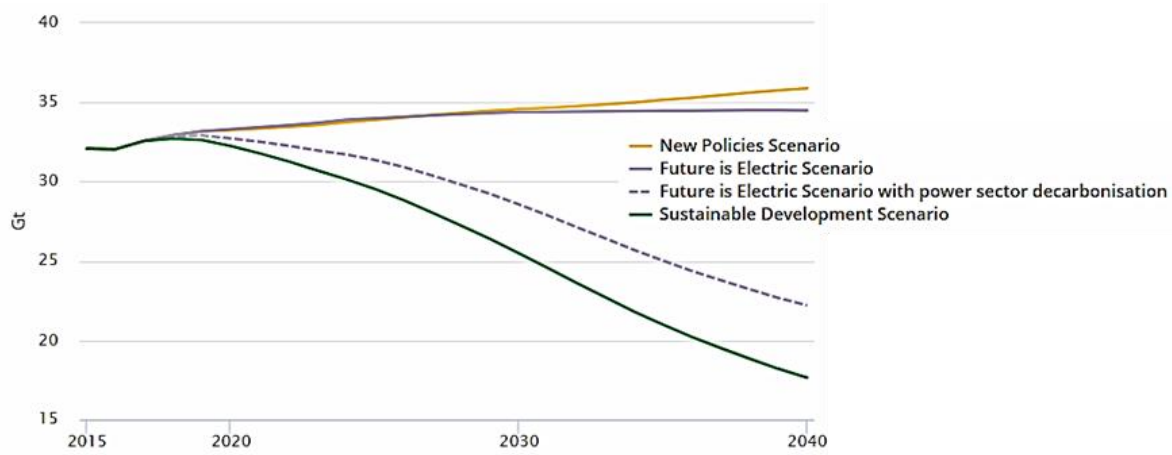

Figure 1.1: Energy related CO_2 emissions by scenario

When it comes to storing energy, secondary batteries are one of the most efficient and leading technologies available in today's market. A battery is essentially an electrochemical device capable of converting chemical energy into electrical energy and vice-versa. Lithium-ion battery (LIB) technology is quite mature and has captured the market of portable devices and electric vehicles.

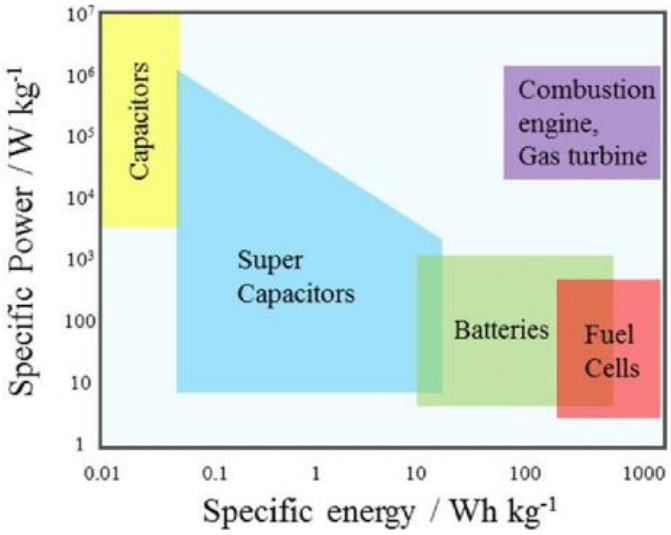

Figure 1.2: Ragone plot of various electrochemical systems

Figure 1.2 shows the Ragone plot, which compares the energy densities and power densities of various electrochemical energy conversion systems. It can be seen that batteries have high energy density, and thus, LIB technology has the potential to be used for grid energy

applications. However, the implementation of LIB for this purpose is limited due to the cost, availibilty and accessability of lithium resources.[3,4] The annual production of $LiCoO_2$ also would not suffice to manufacture the number of electric cars equivalent to the total demand of cars. Hence, the need arose for a battery technology with similar chemistry but more abundant precursors and sodium-ion batteries (SIBs) emerged as the front runner.

1.2 Sodium-ion Batteries (SIBs)

1.2.1 Working of SIB

The operation principle and schematic of SIBs is analogous to LIBs. Figure 1.3 shows a schematic diagram of the basic parts and working of SIBs.

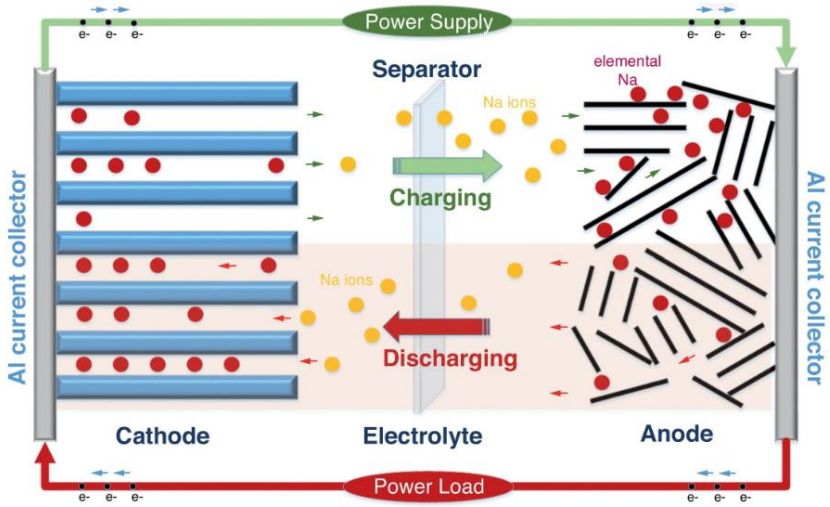

Figure 1.3: Schematic of a sodium-ion battery. Reproduced with permission from Ref [5]., Copyright 2015 Elsevier

It consists of two insertion-based electrodes (positive and negative electrodes) which are separated by an electrolyte. The electrolyte maybe liquid (e.g.- solution containing sodium salts dissolved in aprotic solvents) which requires the use of a porous separator, solid polymer, gel polymer or ceramic electrolytes. The current collector aids in the collection and distribution of electrons throughout the electrodes.[5] In SIBs, during discharge, sodium ions

stored in the negative electrode get released and travel towards the positive electrode through the electrolyte, whereas the electrons liberated at the negative electrode pass through external circuit to the positive electrolyte and reduces the transition metal present in the cathode material. Upon charging, the above-mentioned process reverses. The reactions in a battery are a bulk phenomena, as opposed to the surface phenomenon of capacitors and supercapacitors.

1.2.2 Comparison of LIBs and SIBs

In comparison with their Li-ion counterparts, SIB electrodes have lower electrochemical insertion potential due to lesser reducing potential of Na^+/Na^0 (Table 1.1). The theoretical capacities of the SIB electrodes are also lower due to higher molar mass of sodium in comparison with lithium. However, SIBs are preferred due to the inexpensive and earth abundant sodium precursors in comparison with Li-technology. Besides, the differences in their chemistry can lead to significant difference in terms of insertion potential, stability and diffusion barriers in a given host. A good example of the local coordination preference of Li (octahedral and prismatic) and Na (octahedral and tetrahedral).[6] Table 1.1 summarizes these differences.

Table 1.1: Comparison of sodium and lithium resources and their main properties.

Properties	**Lithium**	**Sodium**
Cationic Radii (Å)	**0.76**	1.06
Potential (V vs S.H.E)	**-3.04**	-2.7
Theoretical Capacity (metal) ($mAhg^{-1}$)	**3829**	1165
World resources (thousands of metric tons)	39500	**>50,000,000**
Cost of carbonates ($/ton)	5000	**150**

The individual electrode potentials and full cell voltages of some popular cathode and anode materials used in SIBs along with their LIB analogues is shown in Figure 1.4. The cell voltage is usually lower for sodium cells.

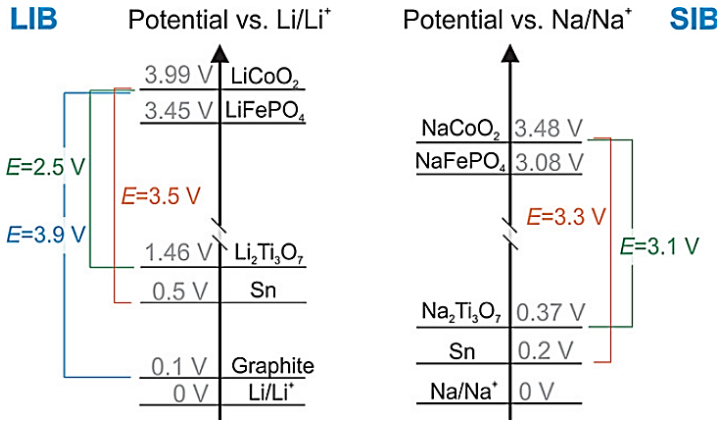

Figure 1.4: Selection of different lithiation/sodiation potentials for a variety of compounds. Reproduced with permission from Ref. [6] Copyright 2017 Wiley-VCH.

1.2.3 General concepts of SIBs

1.2.3.1 Some terms and Formulae

a. Open circuit-voltage (V_{OC}) is given by equation 1.1 and is determined by chemical potentials of anode (μ_A), cathode (μ_C), magnitude of electronic charge (e) and also dependent on the electrochemical window of the electrolyte.[7]

$$V_{oc} = \frac{(\mu_A - \mu_C)}{e} \quad \text{(in V)} \qquad \text{----1.1}$$

b. Theoretical **specific capacity** is the maximum capacity that can be obtained from an electrode. This can sometimes be exceeded[8] by changing the design dynamics of the materials. However, the reported capacity is usually less than the theoretical capacity since the cation cannot be fully removed from the host lattice. It is calculated from the Faraday's law:[9]

$$C_t = \frac{nF}{3.6 * M.W} \quad \text{(in mAhg}^{-1}\text{)} \qquad \text{----1.2}$$

where *n* is the number of reactive electrons per formula unit, *M.W* is the molecular weight of the active material, *F* is the Faraday constant. Energy density is a measure of the energy per unit volume/weight. Gravimetric Energy Density ($Whkg^{-1}$) = Capacity ($Ahkg^{-1}$) $*$ Voltage (V)

c. Gibb's Free Energy (ΔG) determines the feasibility of the reaction in terms of thermodynamics. It is given by equation 1.4. More the negative value of ΔG, the more feasible is the reaction 1.3.[9]

$$Na_{x\ (cathode)} + (y-x)\ Na_{(anode)} \leftrightarrow Na_{y\ (cathode)} + Na_{(anode)} \qquad \text{----1.3}$$

$$\Delta G = \Delta H - T\Delta S = -nFE \qquad \text{----1.4}$$

where T is temperature (in K); ΔH and ΔS are the changes in enthalpy and entropy respectively; *n* is the number of electron transfer involved and *E* is the cell potential. When *n*= *y*-*x*, E is the equilibrium voltage.

d. Coulombic efficiency describes the efficiency by which electrons is transferred in an electrochemical system as a measure of charge (*Q*) lost in one cycle of charge-discharge. The percentage Coulombic efficiency is given by[7]

$$Efficiency = \frac{Q_{discharge}}{Q_{charge}} X\ 100 \qquad \text{----1.5}$$

e. C-rate is the measure at which a battery is charged or discharged. 1 C-rate means it would take 1h to charge/discharge a battery to its maximum capacity. In simple terms, C-is current per unit capacity.[10]

f. Electrochemical window

The safe operation of a battery is dependent on the electrochemical window of the electrolyte. This essentially means that the chemical potentials of the anode and cathode must be such that the μ_A of the anode lies below the LUMO (lowest unoccupied molecular orbital)

of the electrolyte while the μ_C of the cathode lies above the HOMO (highest occupied molecular orbital) as shown in Figure 1.5; otherwise, the electrolyte will be reduced on the anode or oxidized on the cathode to form a Solid-electrolyte interface (SEI). Usually organic electrolytes have larger electrochemical window than aqueous electrolytes and thus are widely used as electrolytes in SIBs.[7,9]

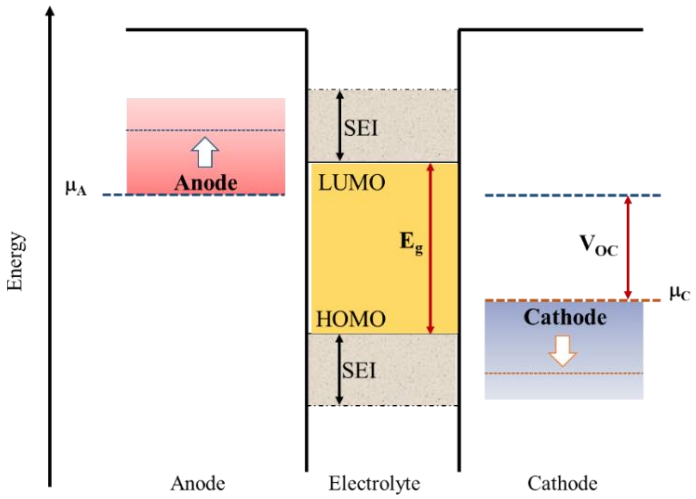

Figure 1.5 Relative energies of the electrolyte window (E_g); μ_A and μ_C are chemical potentials of anode and cathode respectively, V_{OC} is the open-circuit voltage.

g. SEI (Solid-electrolyte interface) is a layer of passivating film formed due to the chemical reactions between the electrode and electrolyte at the electrode surface. They serve a variety of purposes like protecting the electrode from further decomposition while allowing for the Li or Na-ions to diffuse and preventing aggregation of electrochemically active elements on the electrode surface, thus reducing dendritic formation. However, insulating or very thick SEIs may hinder the diffusion process. It also increases the internal resistance of the battery.[9] The observation of a high capacity loss in the first and sometimes in the following cycles (the first cycle may have a capacity beyond the theoretical capacity) is attributed to the SEI formation.

1.2.3.2 Effect of transition-metal and electronegativity

Figure 1.6 (a) shows the increase in the electrochemical potential of cathodes of transition metal elements of the same period and the decrease in the potential as we go down a group. This observation can be explained based on effective nuclear charge. As the effective nuclear charge increases with metal ions in the same period, the valence electron will be held more tightly to the atomic core and requires more energy to promote the electrons from the transition metal orbitals and conversely release more energy when electrons are inserted into the orbitals. Similarly, on going down a group, there is weaker attraction on the valence shell electron, leading to a lower energy for electron transfer and thus corresponding materials have a lower potential. [9]

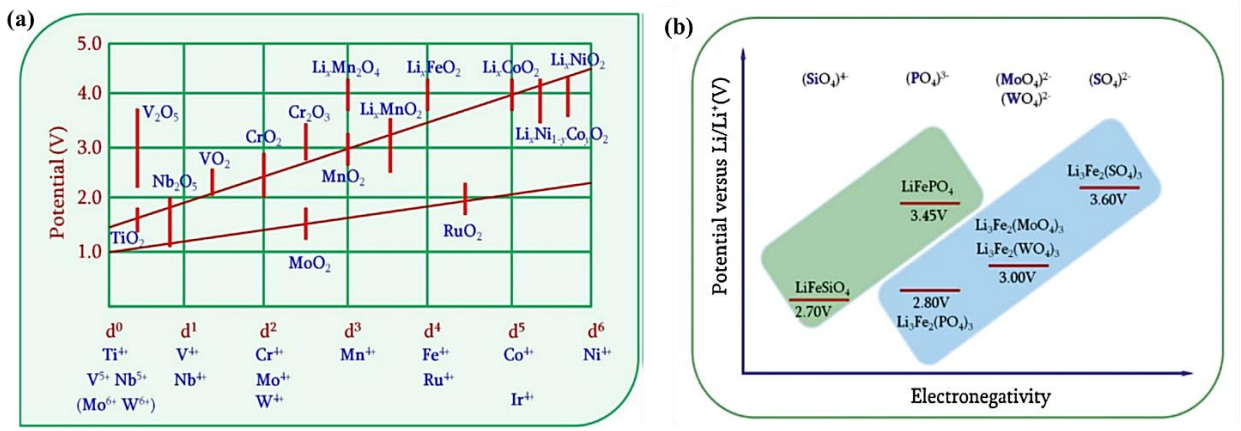

Figure 1.6 (a) Voltage range of some transition metal oxides and (b) electrochemical potentials of ferrous polyanionic compounds. Reproduced with permission from Ref.[9], Copyright 2015 Elsevier.

Figure 1.6 (b) compares the electrochemical potentials of iron polyanionic compounds. On increasing the electronegativity of polyanionic groups, the electrochemical potentials increase due to inductive effect. In transition metal polyanion compounds, the counter-ions (X = Mo, W, S, P, Si) share the corner oxygen with the transition metal cations in the M–O–X-O-M linkages. The inductive effect of X pulls some charge density out of M–O bonds which

leads to decrease in orbital overlap of M and O and contributes to the ionic character of the bond. Similarly, fluorides possess higher electrochemical potential than polyanionic compounds due to the strong inductive effect of fluorine. Also, polyanions have better thermal stability than their oxide counterparts.[11]

1.2.3.3 Effect of other factors

Substitution and doping are other methods of increasing the capacity of the cell. It generally employs the idea of substituting with a transition metal that forms stronger bonds with the framework or by replacing it with a lower oxidation state redox pair such that the structure can be maintained while allowing more sodium ions to be imbibed into the same unit cell to maintain charge neutrality.[12] Doping with electrochemically inactive materials like Al and Mg sometimes help in stabilizing the structure.[13,14] Most of the electrode materials are inherently not good electrical conductors. Hence, conducting carbon is mixed during electrode preparation.[15] Size reduction leads to higher power density due to shortened 1D ion channels but lower volumetric energy density as the surface area increases for electrode/electrolyte interaction.[16]

1.2.4 Popular cathode materials used in SIBs

The “know-how” knowledge gained from LIB electrode materials can be extended to synthesize SIB electrode materials. This has led to study of analogous systems, some of which are promising as cathode materials for SIBs. Figure 1.7 shows the current state-of-art SIB cathode materials. A few of these classes of compounds have been described within this section.

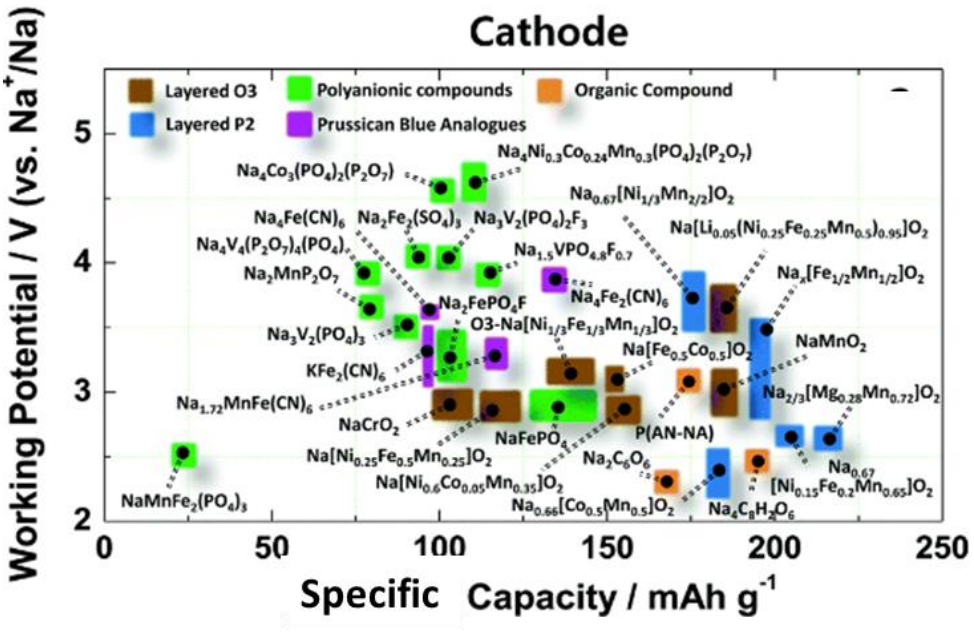

Figure 1.7 State-of-the art cathode materials, Reproduced with permission from Ref.[3], Copyright 2017 Royal Society of Chemistry

1.2.4.1 Two-Dimensional Layered Oxides

Layered oxides consist of 2D layers of transition metal oxides and sodium ions occupy the space between the interlayers. These materials are known to stabilize in different structures (some of which are O3, P3, and P2) as shown in Figure 1.8. Symbol of "P" or "O" represents a prismatic or octahedral coordination environment of Na^+ ions, the "2" or "3" suggests the number of unique transition metal layers in a single cell unit. O3-Na_xTMO_2 (space group: *R3m*) has layers arranged in AB, CA, and BC stacking in the unit cell while P2 phase (space group of $P6_3/mmc$) has an AB-BA-AB arrangement. Also, sodium in P2-type occupies two sites: Na1 contacts two TMO_6 octahedra of the adjacent slabs along its face, whereas Na2 contacts the six surrounding TMO_6 octahedra along its edges.[17] The O3 and P2 layered oxides show promising capacities. However, due to these phases being composition and temperature sensitive, there are plenty of hurdles to synthesize them as single phases. P2-type is usually formed above 700°C and Na content from 0.58-0.66. Below this temperature and

composition, there is an intergrowth of P2 and P3 phases. O3 phase is formed at a high temperature of around 900 ^{o}C and Na content close to 1.[18] P2-type cannot be stabilized with a Na stoichiometry larger than $Na_{2/3}MO_2$, which may be due to the high Coulombic repulsion between the two Na sites (they cannot be occupied simultaneously).

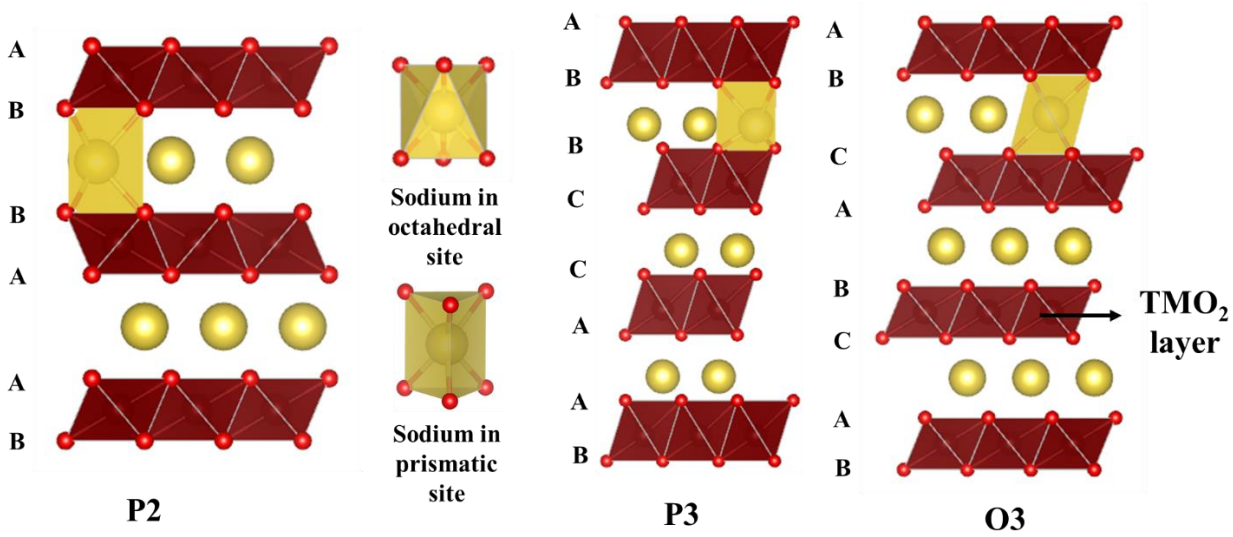

Figure 1.8: Crystal structures of P2, P3, O3-layered oxides

Figure 1.9 shows a typical charge-discharge profile of layered oxide. It has a multi-step staircase-voltage profile which is due to the successive phase transformation during sodium (de)-intercalation. *In-situ* XRD experiments, coupled with electrochemical studies confirmed the successive phase transition on these layered structures. The gliding of TMO_2 slabs in O3 structure follows as O3 ↔ O'3 ↔ P3↔ P'3. The O3 structure transforms to P3 when Na content is ~ 0.5, thus only half of the theoretical capacity can be reached. The phase behavior of $NaCoO_2$ has been thoroughly studied by Delmas *et al*. in 2010.[19] Other single transition metal layered oxides include Na_xTiO_2, Na_xVO_2, Na_xCrO_2, Na_xMnO_2 and Na_xFeO_2 (70-100 $mAhg^{-1}$) and they have similar voltage profiles.[20] A much smoother voltage profile can be obtained by substitution of the transition metal like Ni in $Na_xMn_xNi_{1-x}O_2$ as there is no Jahn Teller distortion of Ni^{2+}. This also gave a higher specific capacity of 135 $mAhg^{-1}$.[21] Ternary

systems like $NaNi_{1/3}Mn_{1/3}Co_{1/3}O_2$ (NaNMC), has also been studied. Originating from the $Ni^{4+/2+}$ redox reaction, the cathode delivers a reversible capacity of 120 $mAhg^{-1}$ (i.e. 0.5 moles of Na^+ ions) within the voltage range of 3.75–2.00 V at 0.1 C.[22]

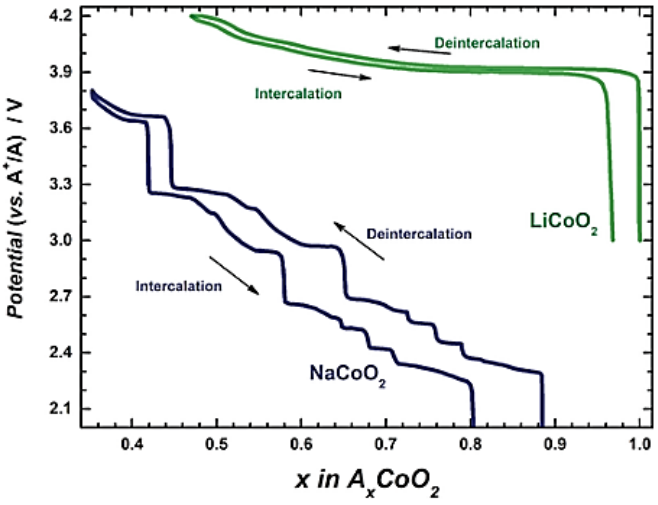

Figure 1.9 Voltage profiles of $Li/LiCoO_2$ and $Na/NaCoO_2$ cells. Reproduced with permission from Ref. [19] . Copyright 2010 Springer Nature

1.2.4.2 Three-Dimensional Polyanionic Compounds

Three-dimensional transition metal polyanionic frameworks has the advantage of enhanced structural stability and higher operating potentials in comparison their oxide counterparts. Figure 1.10 shows the structures of some of the stellar polyanionic cathodes recently reported for SIBs. The olivine structured $LiFePO_4$ is successfully used in commercial LIBs,[23] while its sodium counter-part $NaFePO_4$ stabilizes in the electrochemically inactive maricite structure.[24] The sodium ion containing olivine Na_xFePO_4 polymorph can be prepared from the lithium analogue by electrochemical displacement of Li^+ and has a discharge capacity of 111 $mAhg^{-1}$ at 0.1C.[25] As alternatives, vanadium-based cathode materials such as the NASICON (Na Super Ionic CONductor) with composition $Na_xV_2(PO_4)_3$ (NVP) have been studied. NVP was initially synthesized by Delmas *et al.*[26] and it exhibits interesting electrochemical properties; two plateaus are observed at 3.4 V and 1.6 V vs. Na^+/Na^0

associated with the V^{4+}/V^{3+} and V^{3+}/V^{2+} redox reactions, respectively, in total allowing the extraction of 1.7 Na from $Na_3V_2(PO_4)_3$.[27] Shakoor *et al.* studied the electrochemical sodium intercalation properties of $Na_3V_2(PO_4)_2F_3$ through combined computational and experimental efforts. This cathode showed two voltage plateaus (~3.7 and 4.2 V vs. Na^+/Na^0) with reversible capacity of ~120 $mAhg^{-1}$ at C/20 rate.[28] Pyrophosphate compounds are another class of materials which exhibit high intercalation potential and is made of transition metal based MO_6 octahedra and P_2O_7 units. $Na_2FeP_2O_7$ cathode has been showed to have a reversible capacity of 82 $mAhg^{-1}$ when cycled at a rate of C/20; with a step-wise voltage curve (~2.5 and 3.0 V vs. Na^+/Na^0) through the redox activity of Fe^{3+}/Fe^{2+} couple.[29] $Na_4Co_3(PO_4)_2P_2O_7$ has multiple redox activity in the potential region between 4.1 V and 4.7 V and can deliver a reversible capacity of 95 $mAhg^{-1}$ at the current density of 0.2 C, corresponding to 2.2 Na^+ extraction and insertion.[30]

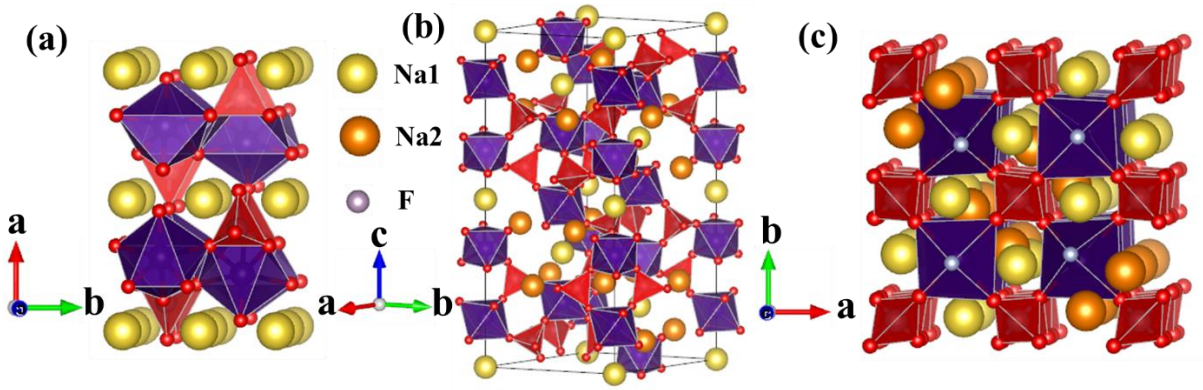

Figure 1.10 Crystal structures of (a) olivine-NaFePO4 (b) $Na_3V_2(PO_4)_3$ (c) $Na_3V_2(PO_4)_2F_3$ (red tetrahedra is PO_4 and purple octahedra represents VO_4 or VO_4F_2)

1.2.4.3 Three-Dimensional Metal Oxides

$LiMn_2O_4$ is an attractive cathode material because of the redox activity of Mn around 4.0 V vs. Li^+/Li^0 and a specific capacity of ~110 $mAhg^{-1}$ against its theoretical capacity of ~140 $mAhg^{-1}$.[31,32] Unfortunately, the sodium counterpart, $NaMn_2O_4$ crystallized in $CaFe_2O_4$-type

structure and can only be synthesized under high pressure and temperature.[33] It exhibits a capacity of only about 65 $mAhg^{-1}$ at a current of 5 mAg^{-1} in the voltage range of 2.0–4.0 V. Also, the redox potential of Mn is observed at about 3.0 V vs. Na^+/Na^0 as compared to 4.0 V vs. Li^+/Li^0 for $LiMn_2O_4$.

1.3 Characterization Techniques Used

1.3.1 Cyclic Voltammetry (CV):

Cyclic voltammetry (CV) is a dynamic electrochemical method for acquiring qualitative and quantitative information about the redox processes occurring within an electrochemical cell by scanning the potential (Figure 1.11 (a)) at a given sweep rate (usually measured in mV/s) and recording the resulting current. The potential sweep starts from the initial open circuit potential OCV (Open Circuit Voltage) to desired potential E1. Subsequently the scanning direction is reversed to reach another potential E2.

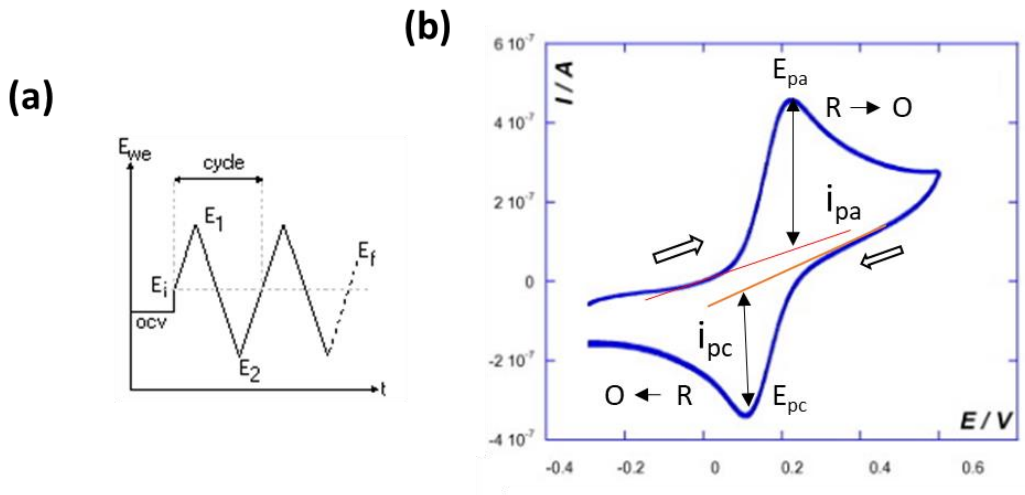

Figure 1.11: (a) Schematic showing the voltage sweep profile of CV and (b) a typical CV graph

Figure 1.11 (b) shows a representative CV graph. On charging, voltage is swept to the positive side. When oxidation occurs, there is a loss of electron leading to a positive jump in current value and a corresponding peak is observed in the CV graph. The corresponding

current is called anodic current. Similarly, a peak with negative current value (called cathodic current) is observed at the reduction potential (called cathodic potential) of the redox species.[34]

1.3.2 Galvanostatic Cycling with Potential Limitation (GCPL)

GCPL is a chrono-potentiometric technique. A constant current (*i*) is applied to the working electrode and its potential is recorded as a function of time.[35] The current is positive during charge and negative during discharge. By GCPL, the specific cell capacity and stability upon cycling can be assessed. Also, differences in the coulombic efficiency can be obtained from these measurements. It provides us with additional information about the presence of any irreversible additional redox process such as electrolyte decomposition or SEI formation.

1.3.3 X-Ray Diffraction (XRD)

1.3.3.1 Principle

Radiation incident upon a crystal is scattered in a variety of ways. When the wavelength of the radiation (λ) is on the same scale as the atom spacing in a crystal, the scattering which is termed diffraction, gives rise to a set of well-defined beams arranged with a characteristic geometry, thus forming a diffraction pattern. X-ray diffraction data collection is the result of relative intensity for each reflection with a set of planes in crystal, known as Miller indices (h, k, l) along with the corresponding scattering angle (2θ) for that reflection. The positions and intensities of the diffracted beams are a function of the arrangements of the atoms in space and some other atomic properties. The condition for diffraction is given by Bragg's law:[36]

$$n\lambda = 2d_{hkl}\, sin\theta$$

where n = an integer, for peak order, λ= wave length of the radiation (X-ray), d_{hkl} = interplanar spacing of the hkl planes in the crystal lattice, θ = diffraction angle. A diffraction pattern is obtained only during constructive interference as shown in Figure 1.12.

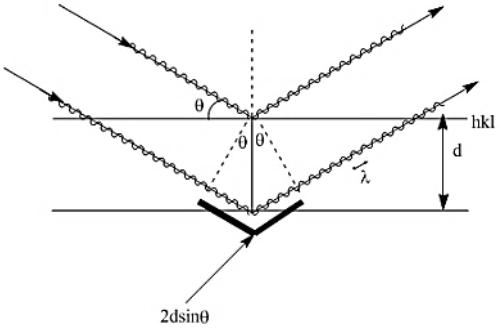

Figure 1.12 Schematic diagram of Bragg's law

1.3.3.1 Rietveld Refinement

It is a refinement technique which is used to fit the experimental XRD pattern based on known structure models by simulating an XRD profile until it matches the measured profile. It uses a least-square method for refinement around a local center. It reaches the next minimum available from the starting point and hence cannot be used when to find a global minimum over the full range of the sin function. Thus, it is important to have a starting model as close to the calculated model. The height, width and position of the reflections in the XRD pattern can be used to determine many aspects of the material's structure. It was first described by Hugo Rietveld in 1969.[37] These days many software, like GSAS[38] and FULLPROF[39], have been developed to incorporate the many parameters that can be changed for a better fit. The parameters which are refined during the fitting includes peak shape, wavelength, atomic coordinates and their occupancies, background, addition of a different phase and so on.

Rietveld discrepancy values: χ^2 and R-factors: Figure 1.13 shows an example of Rietveld refined pattern. The Bragg's positions are the theoretically determined reflections that should arise from the space group using the Bragg's law.

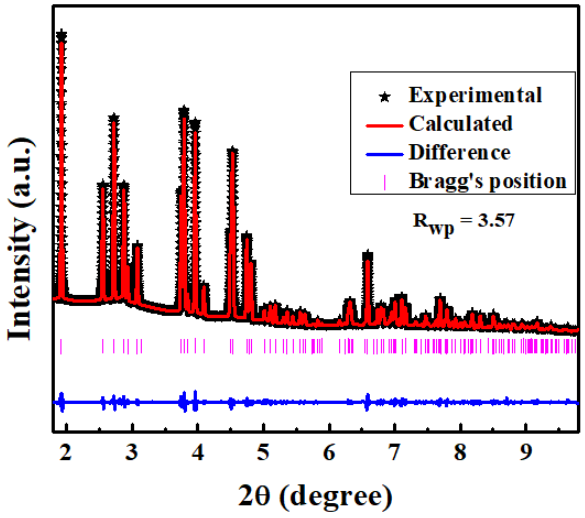

Figure 1.13 Sample Rietveld refined pattern

Let the observed or experimental intensity value be determined as $Y_{O,i}$ and the calculated intensity of our model be $Y_{C,i}$ where *i* indicates the intensity was measured at $2\theta_i$. The uncertainty estimates for $Y_{O,i}$ can be labelled as $\sigma[Y_{O,i}]$ which is required to calculate the weight W_i, $[= 1/\sigma[Y_{O,i}]^2]$. Rietveld programs optimize the model function by minimizing the weighted sum of squared differences between the observed and calculated intensity values, i.e., to minimize $\Sigma\,[W_i\,(Y_{C,i} - Y_{O,i})^2]$. The **Weighted profile R-factor, R*wp***, is given by:

$$\boldsymbol{Rwp} = \frac{\sum \boldsymbol{W_i}\,(\boldsymbol{Y_{C,i}} - \boldsymbol{Y_{O,i}})^2}{\sum \boldsymbol{W_i}\,(\boldsymbol{Y_{O,i}})^2}$$

Expected R factor (R*exp*) is calculated assuming the model is a perfect fit. For an ideal fit, thus the intensities will be equal. $Rexp^2 = \frac{N}{\sum \boldsymbol{W_i}\,(\boldsymbol{Y_{O,i}})^2}$ where *N* is the number of data points.

$\boldsymbol{\chi^2}$ is a statistical value obtained by $[Rwp\ /Rexp]^2$. $\chi 2$ should be as close to 1 as possible for a good fit.[40]

Chapter 2

High Voltage $NaCoPO_4$ Cathodes for Rechargeable Sodium-ion Batteries

2.1 Introduction

The quest for cleaner and more efficient energy is never ending. One way to achieve this is by improving the storage and conversion devices. Batteries are energy storage devices which have advantages like high round trip efficiency, low maintenance and flexible energy and power densities.[41] Modern lithium-ion battery (LIB) technology is quite mature and has captured the market of portable devices and electric vehicles. However, to use them for grid storage applications, there remains the question of cost, availability and accessibility of lithium resources.[4] In contrast, sodium sources are abundant, widely available and inexpensive. Thus, it has the potential to be used in large scale applications.[42]

A possible strategy to find suitable cathode materials for sodium-ion batteries (SIBs) is to implement the 'know-how' knowledge gained from LIBs. Though intercalation electrode materials could be used in both LIBs and SIBs without greatly affecting the energy density (only a fraction of the active mass is from Li or Na), it is necessary to note the differences in their chemistry. Lithium has a higher electrode potential than sodium (–3.04V vs. S.H.E., compared to –2.71 V vs S.H.E.) as well as smaller cationic radius (0.76 Å vs 1.06 Å of Na^+).[4,41] Thus, it leads to a significant difference between lithium and sodium intercalation chemistry in terms of insertion potential, stability and diffusion barriers in a given host. For

instance, the migration barrier for lithium and sodium ions in layered oxides is comparable while in the close packed MPO_4 framework, sodium ions have high energy diffusion barrier and exhibit sluggish kinetics which is also observed experimentally.[17,43] From a synthesis point of view, replacing smaller lithium ions by larger sodium ions may also result in different thermodynamically stable structures which may or may not possess diffusion channels for larger sodium ion. A classical example could be $AMPO_4$ (M = Fe, Mn, Ni) family of compounds in which Li-based compounds crystallizes in olivine-type structure containing 1D diffusion channels[23], whereas Na- bearing compounds stabilizes in maricite-type structure, which do not have any sodium ion conducting channels.[44,24] The olivine $NaFePO_4$ structure has been shown to be achieved by techniques like sodium intercalation into de-lithiated $LiFePO_4$ which has a discharge capacity of 111 $mAhg^{-1}$ at 0.1C.[25]

On extending the study to cobalt, $NaCoPO_4$ is found to have the uniqueness of crystallizing into four different structures (Figure 2.1), The first of these polymorphs is α-$NaCoPO_4$ which crystallizes in the space group *Pnma* wherein cobalt is in octahedral coordination. This is reported to be the thermodynamically most stable structure and is formed at 650 ^oC. It reversibly transforms to β-$NaCoPO_4$ at 725 ^oC.[45,46] Also known as 'blue' phase, this structure crystallizes in $P6_5$ space group with cobalt at tetrahedral site. Another polymorph showing the same tetrahedral coordination of cobalt is structurally similar to ABW zeolite (space group $P2_1/n$).[47] The last polymorph, known as the 'red' phase (space group $P2_1/c$) is the most peculiar with cobalt in unusual trigonal-bipyramidal coordination to form 1D-channels for cation diffusion.[48,49] It is also worth noting that only α- and β- phases were prepared as single phase powder samples[45] while the other phases were reported to be synthesized in mixtures of cobalt phosphate polymorphs.

Differential scanning and high-temperature oxide melt drop solution calorimetry techniques were carried out to determine the relative stability, and enthalpy of formation of the α-, β- and red- phases. Kimura *et. al.*[50] studied magnetoelectricity in β- $NaCoPO_4$. Recently Selvan *et. al.* reported it as a potential electrode material for hybrid supercapacitors.[44] α-$NaCoPO_4$ has been used studied as a bifunctional catalyst for water-splitting systems.[18, 51] The metastable red-phase has been characterized as a high voltage (4.1 - 4.4 V) sodium battery cathode.[49] Initial structural and electrochemical characterizations on some of these polymorphs were done by P. Vajeeston *et.al.*[52]

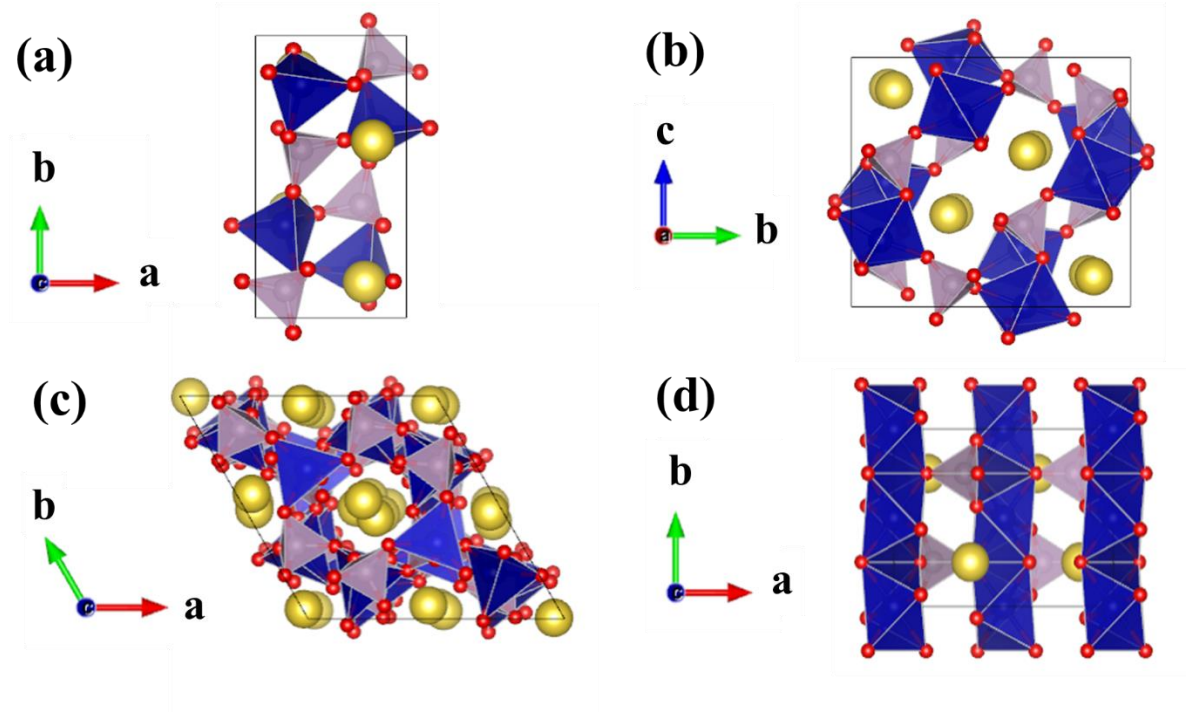

Figure 2.1: Crystal structures of (a) ABW-$NaCoPO_4$; (b) 'red'-$NaCoPO_4$; (c) β-$NaCoPO_4$ and (d) α-$NaCoPO_4$ (yellow atoms- Na, grey- phosphate tetrahedra, blue- cobalt polyhedral)

In the present study, we have attempted to understand the formation mechanism of $NaCoPO_4$ family of compounds using temperature dependent *in-situ* Powder X-Ray Diffraction (PXRD) measurements. Two interesting observations were made, viz., (1) the formation of β-$NaCoPO_4$ at a temperature lower than previously reported and (2) the difference in the

XRDs of the *in-situ* high temperature γ–$NaCoPO_4$ polymorph and the quenched sample at the same temperature. The insights gained from these studies also helped us to synthesize α-, β- and ABW- $NaCoPO_4$ polymorphs and evaluate their electrochemical sodium (de)-intercalation properties. We also attempt to support our studies with DFT calculations.

2.2 Experimental Section:

2.2.1 Synthesis:

Two types of precursor mixtures were used in this study; precrusor-1 consist of NaH_2PO_4 (Sigma-Aldrich, 99%) and $Co(OH)_2$ (Sigma-Aldrich, 99.9%) whereas precursor-2 is made of NaH_2PO_4 and $CoCO_3$ (Alfa-Aesar, 99.5%). Initially the precursor mixtures were ballmilled in a mole ratio of 1:1 for 30 mins in a high energy SPEX Sample Prep Mixer/Mill 800M. These precursors were used directly for the temperature dependent *in-situ* XRD studies between 30 ^oC to 765 ^oC.

Precursor-2 was used to synthesize: (a) β-$NaCoPO_4$ by heating it to 350 ^oC for 6 hours. (b) α-$NaCoPO_4$ by annealing it to 650 ^oC for one hour and (c) β-NaCoPO4 (quenched at high temperature) by heating it to 750 ^oC and subsequently quenching it to room temperature using liquid nitrogen. Precursor-2 was used similarly to synthesize the same polymorphs at the given temperatures. In addition, precursor-1 was used to synthesize ABW-$NaCoPO_4$ by heating it at 150 ^oC for 12 hours.

2.2.2 Temperature dependent *in-situ* XRD measurement:

Temperature dependent *in-situ* XRD measurements were done at PETRA-III (Beamline P02.1) of DESY, a member of the Helmholtz Association (HGF), using a monochromatic radiation of 60 keV and wavelength of 0.207 Å. The samples were loaded into a capillary on top of a rotating sample holder and heated by a hot-air blower at close proximity at the rate of

5 ºC/min. The data was acquired every five minutes including the acquisition time of 50s per pattern. Data was also acquired during the cooling process to room temperature. Initially, a heating experiment was performed on silicon powder (NIST SRM-640e) which served as the reference material to calibrate the temperature as shown in Figure 2.2. The cell parameter values for reference was taken from Ref. [53]. The raw data was obtained as Debye-Scherrer rings, which were integrated into XRD patterns using Fit2D by using the same silicon standard. The XRD patterns were fitted by Rietveld analysis using FullProf[39] by using ABW-$NaCoPO_4$ (ICSD collection code-280175); (b) 'red'-$NaCoPO_4$ (ICSD collection code-84709); (c) β-$NaCoPO_4$ (ICSD collection code-82753) and (d) α-$NaCoPO_4$ (ICSD collection code-82752) as the starting models respectively.

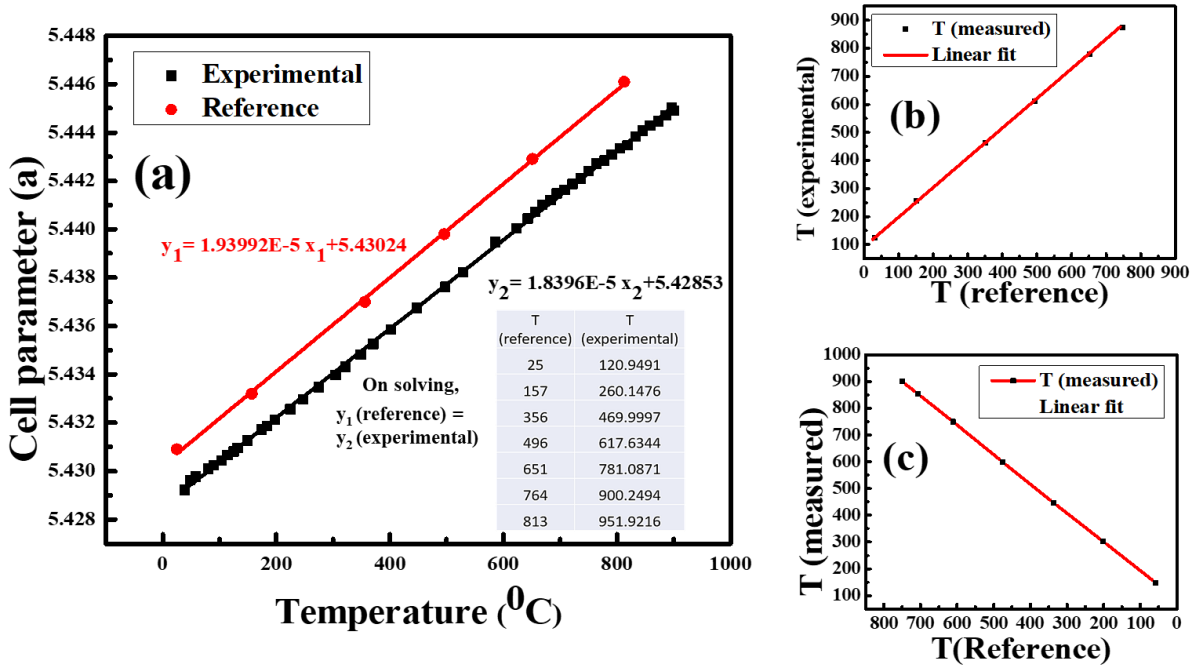

Figure 2.2 (a) Temperature calibration by comparing cell parameters of silicon reference: (b) during heating from 30 ºC to 765 ºC and during cooling from 765 ºC to 30 ºC.

2.2.3 Electrode preparation:

All electrochemical tests were carried out using a Swagelok cell using sodium metal (Sigma 99%) as the counter electrode. The working electrodes were prepared by ball-milling 70 wt% of $NaCoPO_4$ phase 22 wt % of TIMICAL SUPER C-45 carbon (MTI) and 8 wt% of poly(vinylidene fluoride) (Sigma-Aldrich) for 30 minutes and then making a slurry in N-methyl pyrrolidine which was coated on a 0.025mm thick carbon-coated aluminum foil current collector. The electrode laminate was dried at 70 ^oC in a vacuum over for overnight and punched as a disk (10 mm diameter) and contained a actives mass of ~ 2.0 mg cm^{-2}. The electrolyte contained 1.0 M $NaClO_4$ in a mixture of ethylene carbonate, propylene carbonate, dimethyl carbonate (45:45:10 in wt %) with 2% FEC. The assembled cells were cycled against sodium metal at C/25 in the range of 4.7-2.0 V vs. Na^+/Na^0.

2.2.4 DFT calculation for enthalpy of formation-

The enthalpy of formation ΔH_f of a chemical species provides a basis for understanding its thermodynamic stability and also helps to differentiate between different phases by constructing a phase diagrammatic representation of the energies. ΔH_f is essentially the change in enthalpy accompanying the formation of 1 mole of the species in its standard state from its constituent elements in their standard state (1bar, 298 K).

Thermodynamically, the enthalpy of formation is calculated as:

$$\Delta H_f = \frac{1}{n}[E_s - \sum x_i E_i],$$

where, E_s *is* the total energy of the species, E_i is the energy of the i^{th} constituent element, and x_i is its mole fraction. The enthalpy of formation is standardized per total number of atoms in the unit cell considered.

For the $NaCoPO_4$ systems, the enthalpy of formation can be calculated as follows:

$$\Delta H_f = \frac{1}{n}[E_{sp} - E_{Na} - E_{Co} - E_P - E_O] \quad (1)$$

Where, E_{sp} is the energy of the phase, E_{Na}, E_{Co}, E_P, E_O are the elemental energies equal to 0!. The formation enthalpies can also be calculated as a difference in energies of the $NaCoPO_4$ phase and the precursors involved in the synthesis, namely NaH_2PO_4 and $CoCO_3$, in which case the eq^n. (1) would be written as :

$$\Delta H_f = \frac{1}{n}[E_{sp} - E_{NaH_2PO_4} - E_{CoCO_3}] \quad (2)$$

2.3 Results and Discussions:

2.3.1 *In-situ* temperature dependent XRD

The contour plots of temperature dependent *in-situ* PXRD patterns collected on precursor-1 and precursor-2 from room temperature (RT) to 765 °C are displayed in Figure 2.3.

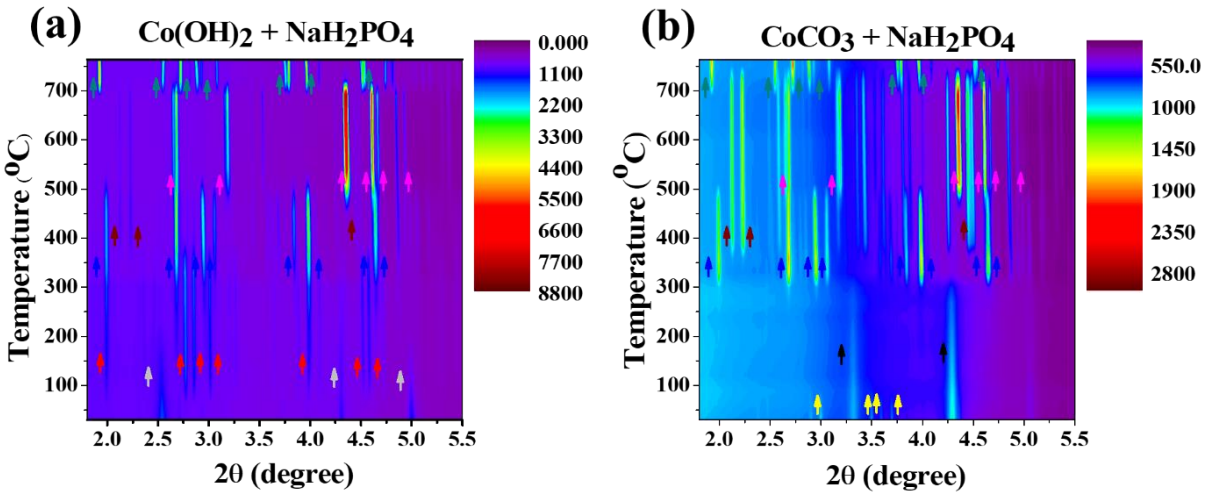

Figure 2.3: Contour plots for *in-situ* XRD patterns upon heating (a) precursor-1 and (b) precursor-2 from room temperature to 765 °C [$NaPO_3$; $CoCO_3$; $Co(OH)_2$; ABW-$NaCoPO_4$; β-$NaCoPO_4$; α-$NaCoPO_4$; mixed phosphate; γ-$NaCoPO_4$]

The presence of different phases, i.e. precursors, $NaCoPO_4$ polymorphs and mixed phosphate ($Na_4Co_3(PO_4)_2(P_2O_7)$), are highlighted by arrows in different colors. The PXRD pattern collected at room temperature on the precursor-2 shows the presence of $CoCO_3$ and $NaPO_3$

(decomposed from NaH_2PO_4) precursors whereas the pattern collected on precursor-1 exhibits only the reflections belonging to $Co(OH)_2$ phase. As the temperature was increased, the first transition from the precursor mixture to the $NaCoPO_4$ phases was noticed at 300 ˚C in the case of precursor-2, whereas the same transition occurred at much lower temperature for precursor-1, at ~ 90 ˚C. Further, the PXRD patterns collected on both experiments showed the presence of similar phases, except the precursor-1 exhibited additional set of reflections in the temperature range of 90-380 °C, which will be detailed in the following section.

To grasp more insights about the reaction mechanism as well as the phases formed during the annealing of precursor-1 and precursor-2, selected *in-situ* PXRD patterns are shown in the range of 2θ = 1.8 to 5.5 in Figure 2.4 and 2.5 respectively.

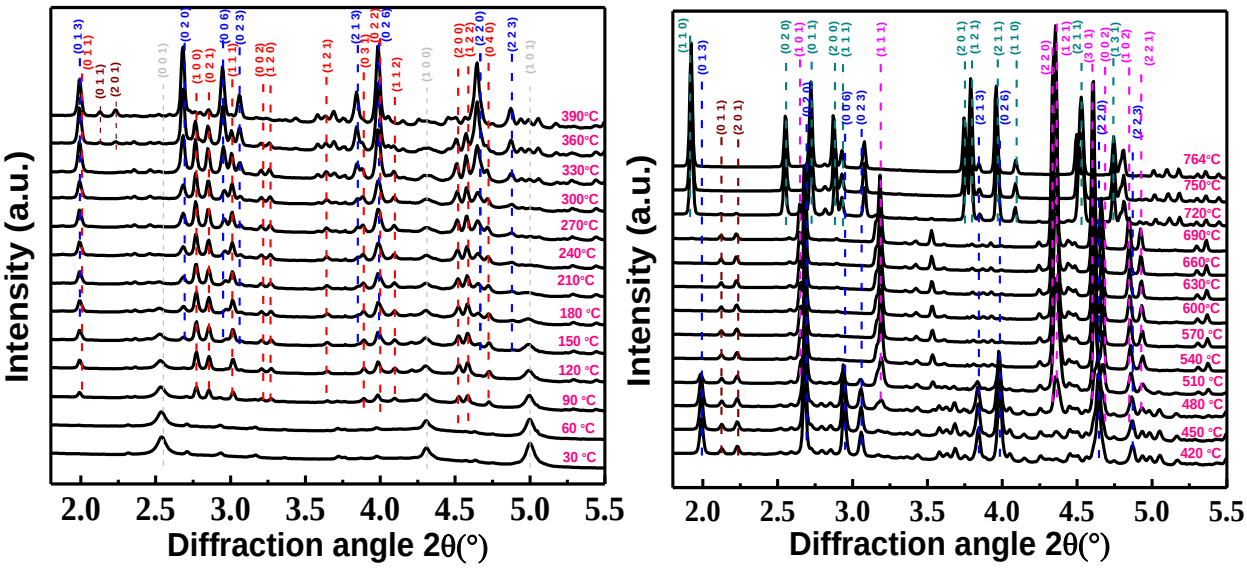

Figure 2.4*:* Selected *in-situ* XRD patterns collected upon heating of precursor-1 from 30 ºC to 765 ºC [--- $Co(OH)_2$, --- β-$NaCoPO_4$, --- α-$NaCoPO_4$, --- mixed phosphate, --- γ-$NaCoPO_4$]

As the temperature is raised from room temperature (RT), the intensities of $Co(OH)_2$ precursor decreased gradually and at ~90 °C, a new set of reflections (indicated by dashed red lines) appeared and started to grow. These new reflections could be fully indexed to the

ABW-$NaCoPO_4$ phase. Another new set of reflections (indicated by dashed blue lines) appeared at ~180 °C which belongs to the β- $NaCoPO_4$ phase. At this point these two $NaCoPO_4$ polymorphs and $Co(OH)_2$ coexist. Once the temperature crosses 360 °C, the appearance of $Na_4Co_3(PO_4)_2P_2O_7$ (called mixed phosphate from here on) and α-$NaCoPO_4$ phases were noticed, as indicated by brown and pink dashed lines respectively. Furthermore, when the temperature is raised above 720 °C, a new set of reflections (indicated by cyan-blue dashed lines) were observed which can be indexed to a new polymorph "γ-$NaCoPO_4$" and the corresponding structural details will be discussed in the next section.

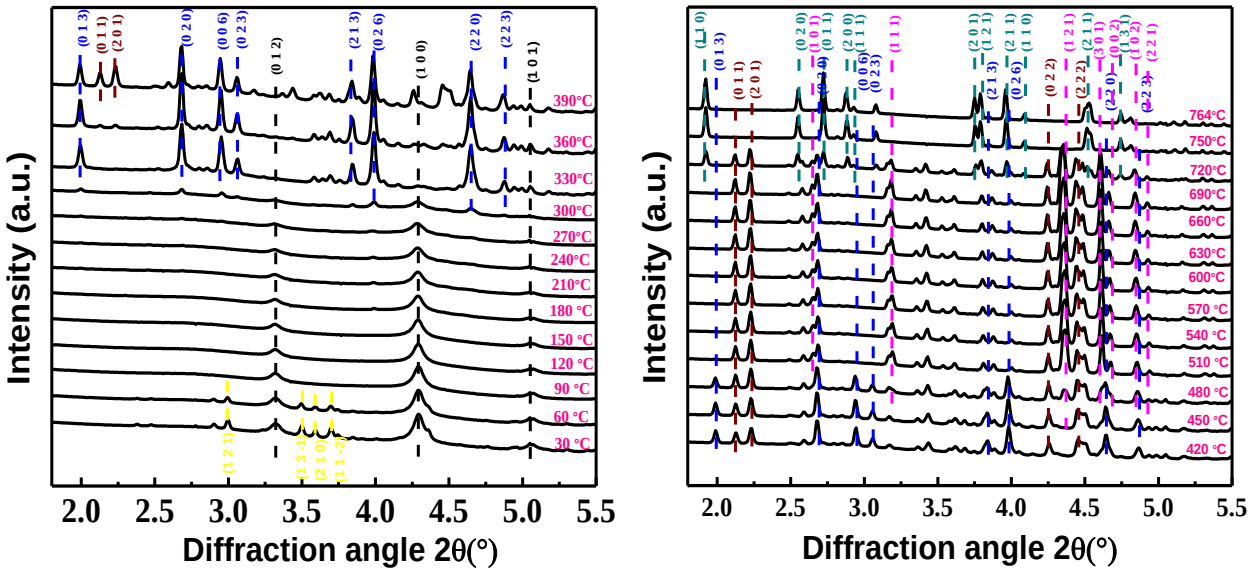

Figure 2.5*:* Selected *in-situ* XRD patterns collected upon heating of precursor-2 from 30 ºC to 765 ºC [--- $NaPO_3$, --- $CoCO_3$, --- β-$NaCoPO_4$, --- α-$NaCoPO_4$, --- mixed phosphate, --- γ-$NaCoPO_4$]

Similar trends on the formation of the $NaCoPO_4$ phases were noticed upon heating the precursor-2 also, except the formation of ABW-NaCoPO4 was missing (Figure 2.5). Finally, the transformation of γ-$NaCoPO_4$ into α-$NaCoPO_4$ and mixed phosphate phases at ~720 ºC was observed upon gradually cooling to RT (Figure 2.6).

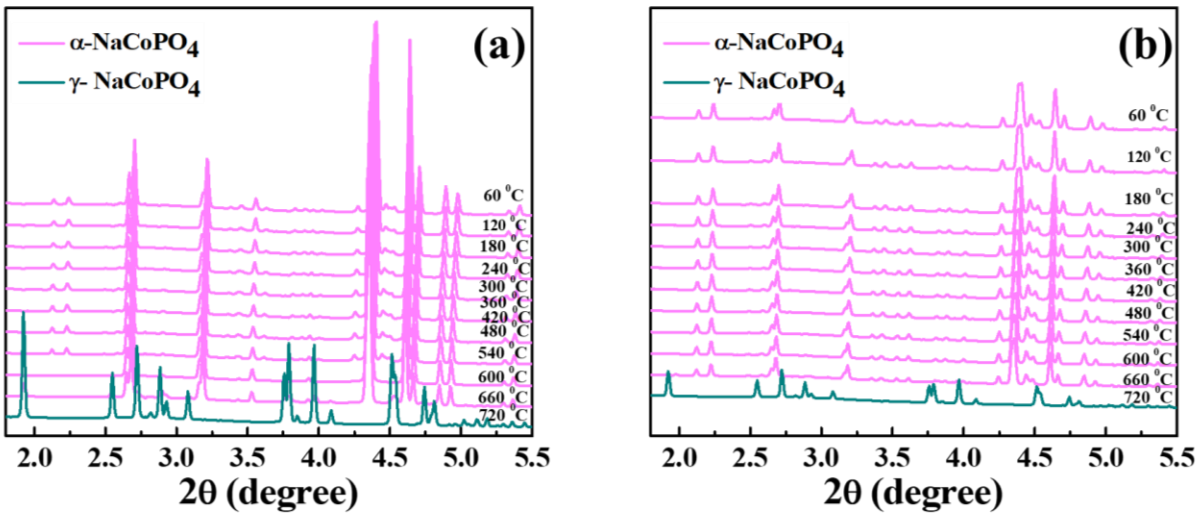

Figure 2.6: Selected *in-situ* XRD patterns upon cooling from 765 ºC to room temperature.

To gain more details on the reactivity of the precursors as well as on the formation mechanism of $NaCoPO_4$ polymorphs, fraction of different phases (%) calculated from Rietveld refinements on the selected *in-situ* PXRD patterns are displayed in Figure 2.7. Few examples of the refinements are also displayed in Figure 2.8.

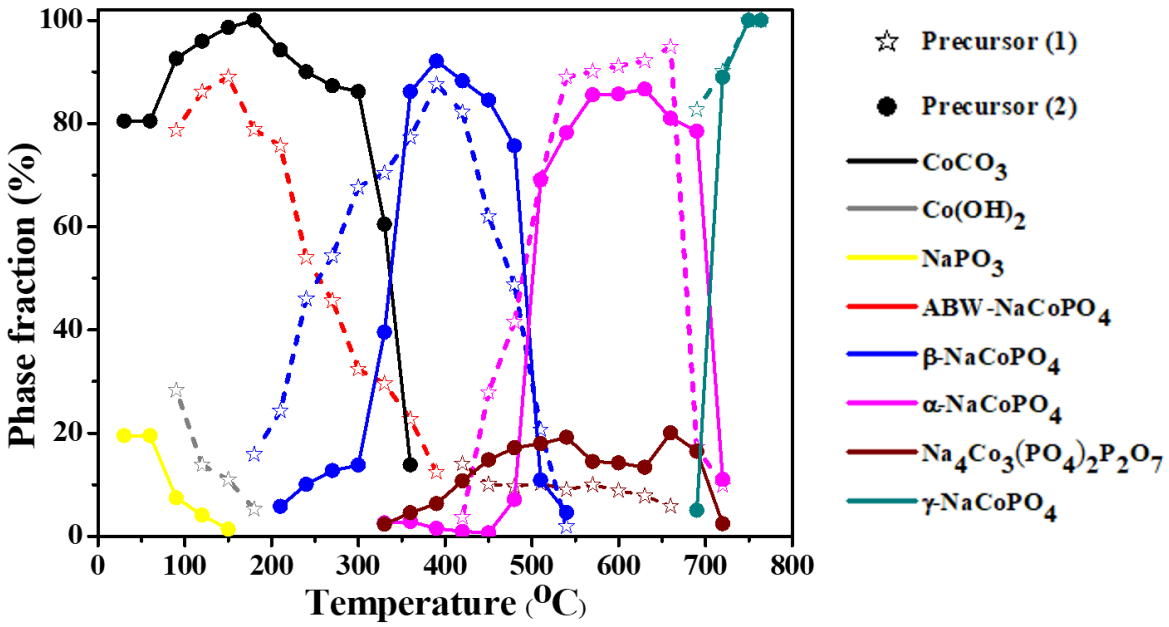

Figure 2.7*:* Phase fraction of the precursors and the different polymorphs of $NaCoPO_4$ in the temperature range of 30ºC to 765ºC during heating.

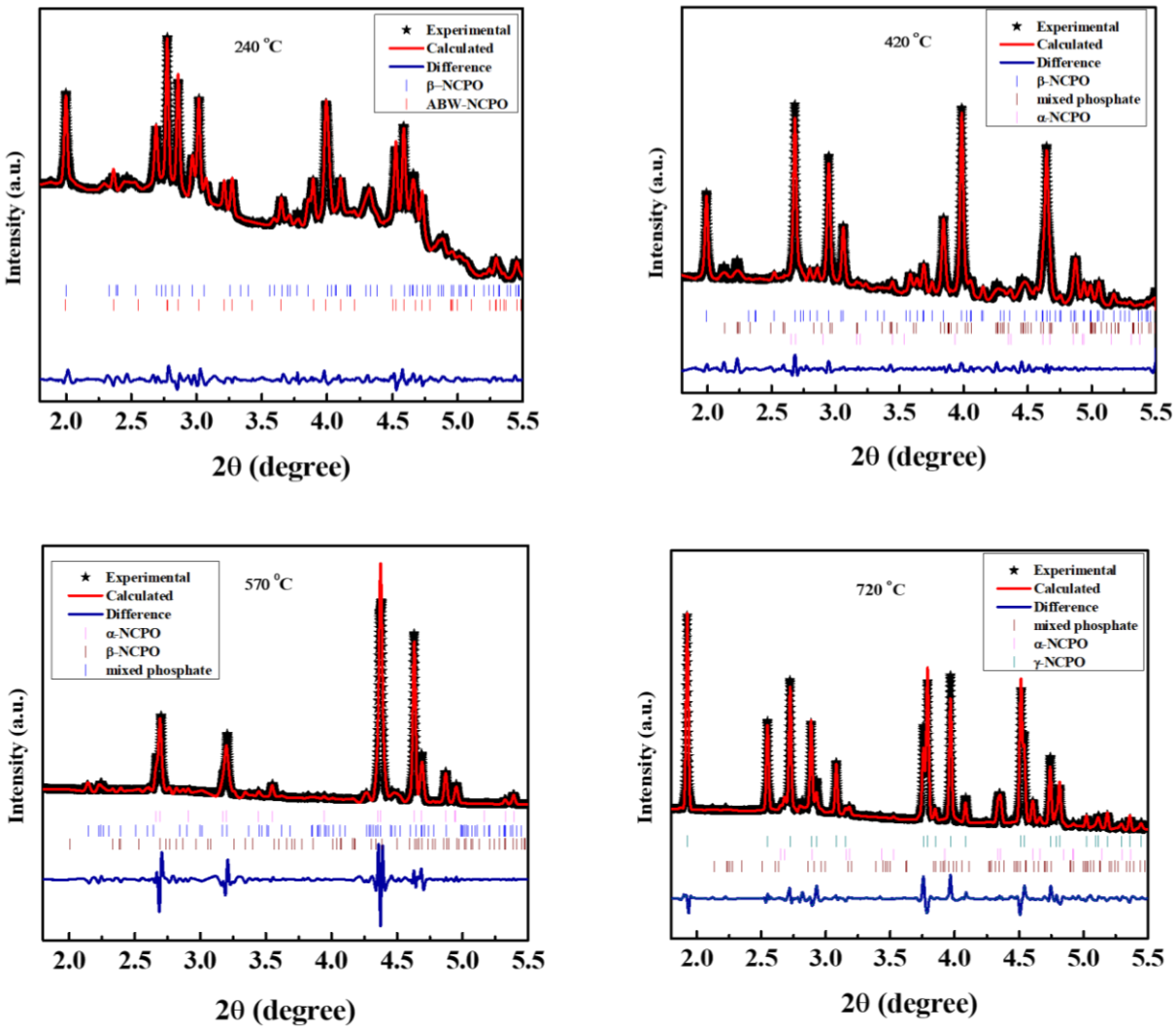

Figure 2.8: Rietveld Refined fitting of some selected *in-situ* XRD patterns having multiple phases.

A clear distinction between the reactivity of the precursors could be made on the formation of the ABW phase. This can be directly correlated to the reactivity and the stability of the precursor and the ABW phase as follows: first, the precursor-2 contained crystalline $NaPO_3$ and $CoCO_3$ phases whereas the presence of $Co(OH)_2$ phase was only noticed in the precursor-1, despite both the mixtures being ball-milled for the same time duration. This could be due to the amorphization of NaH_2PO_4 during ball-milling of precursor-1. Further, the decomposition of $Co(OH)_2$ was initiated and completed below 200 °C along with the formation of the ABW phase. On the other hand, $CoCO_3$ was even stable at ~335 °C which

was the upper limit of the ABW phase stability. The better reactivity of the precursor-1 is also noticed from the formation of different phases at relatively lower temperatures as well as the reduced amount of mixed phosphate when compared to the precursor-2.

In addition to the previous experiments, we have also performed the temperature dependent *in-situ* PXRD studies on the β-$NaCoPO_4$ which was prepared by quenching the precursor-1 (Figure 2.9). Similar to the previous observations, it transformed into α- $NaCoPO_4$ to γ-$NaCoPO_4$ at 480 and 720 °C respectively upon heating from RT to 765 °C.

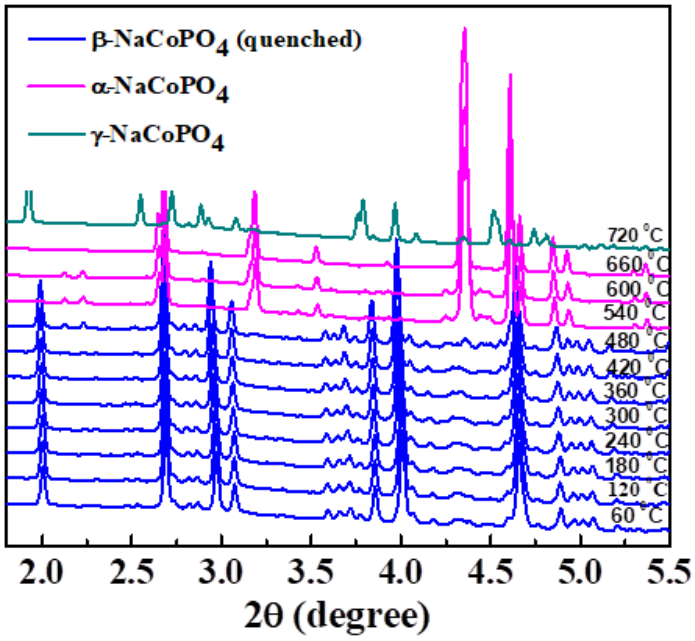

Figure 2.9: Selected *in-situ* XRD patterns for quenched β-NCPO from RT to 720 °C (Formation of γ–NCPO)

2.3.2 Structural analysis

Based on the *in-situ* PXRD studies, we have chosen the synthesis temperatures closer to their maximum presence to make the individual $NaCoPO_4$ phases. Figure 2.10 shows the Rietveld analysis of the $NaCoPO_4$ phase which were synthesized from precursor-1. The corresponding cell parameters, atomic coordinates and Bond Valence Sum (BVS) are displayed in Table 2.1, 2.2 and 2.3 respectively. ABW phase contain CoO_4 and PO_4 tetrahedra which are corner

shared alternatively to make four, six and eight membered rings which result in the formation of the three-dimensional framework.[47]

β-$NaCoPO_4$ was synthesized from the precursor-1 in two ways: by heating the precursor for 6 hours at 350 ^oC and by quenching the product from 750 ^oC. Both attempts yielded single phases. The structure consists of CoO_4 and PO_4 tetrahedra which are corner shared to form six membered rings along *c*-axis.[45] The channels present in between these rings are stuffed with Na^+-ions. Unlike the previous cases, *α*-$NaCoPO_4$ structure consist of Co^{2+} in octahedra environment. The structure is made of edge-shared CoO_6 octahedra running along *b*-axis which are cross-connected by PO_4 tetrahedra and sodium ions are located in 10-coordinate sites.[45]

The crystal structure of high temperature polymorph γ-$NaCoPO_4$ was solved based on $KNiPO_4$[54] with space group $Pna2_1$ and $CsZnPO_4$[55] with space group *Pnma* as model structures. Better agreement between the observed and calculated patterns was found with the former structure (R_{wp} values of 4.95 and 20.7 were obtained for $KNiPO_4$ and $CsZnPO_4$ models respectively). Interestingly, its crystal structure consists of CoO_5 polyhedra which are corner and edge shared with PO_4 units to make six-membered rings along *a*-axis (Figure 2.10 (f)) In between these rings, sodium ions resides in an irregular sevenfold site with Na-O bond lengths varying from 2.5201 to 3.0210 Å. Bond valance sums (BVS = 0.698 A) indicate that this seven-fold Na(1) site is underbonded in comparison with other polymorphs mentioned above and this strong underbonding remains to be the reason for the instability of γ phase at room temperature.

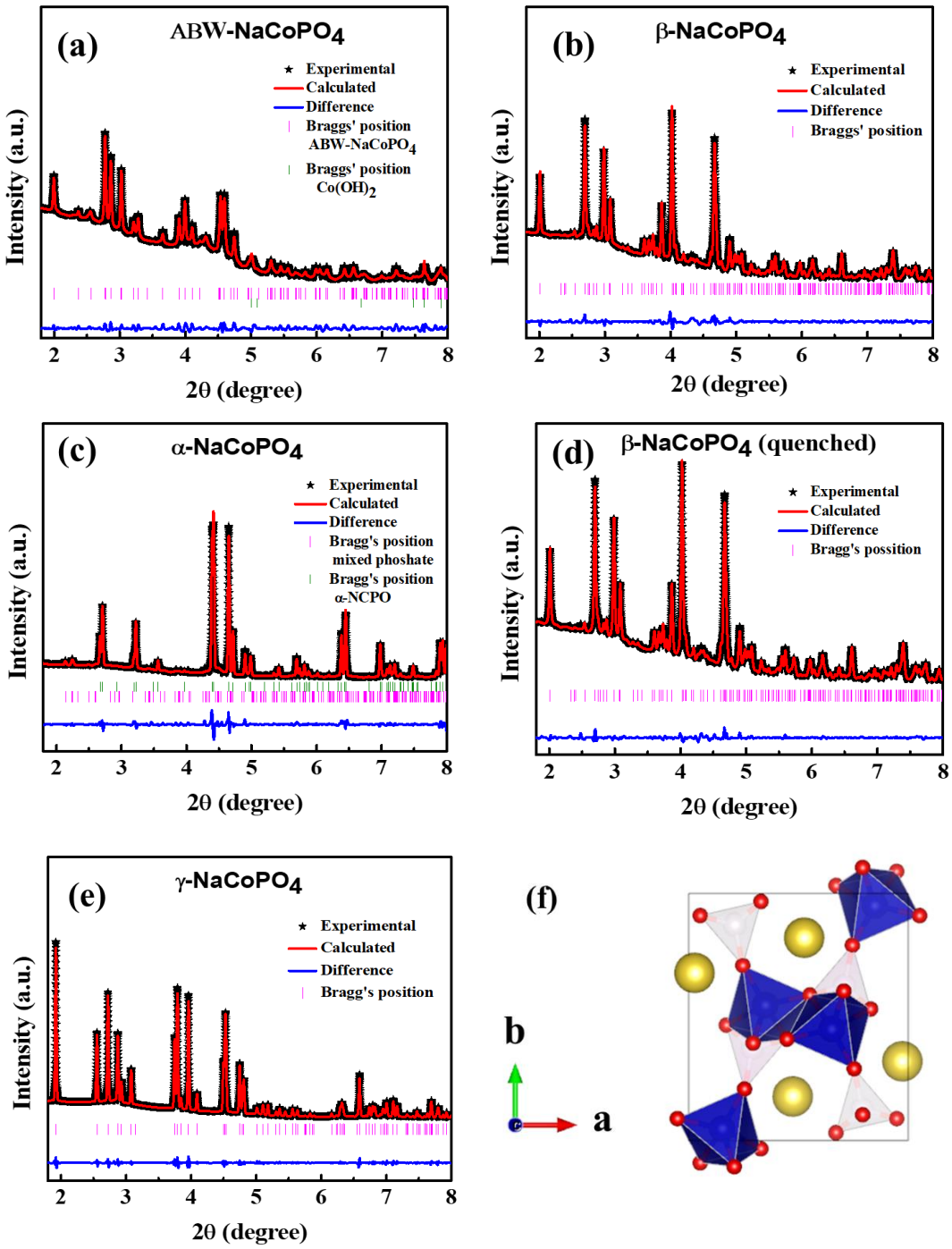

Figure 2.10: Rietveld refinement of room temperature XRD patterns of (a) ABW-$NaCoPO_4$ (b) α-$NaCoPO_4$ (c) β- $NaCoPO_4$-350 ºC (d) β-NCPO-quenched and (e) *in-situ* γ-$NaCoPO_4$ and (f) its corresponding crystal structure

Table 2.1: Calculated Lattice Parameters and Weighted Profile R-Factors (R_{wp})

System	Space group	Lattice parameters		Volume ($Å^3$)	R_{wp}
ABW-$NaCoPO_4$	$P2_1/n$	a= 5.23094 (13) Å b= 10.0079 (8) Å c= 7.38624 (2) Å	α = 90 ° β = 90.155 (19) ° γ = 90 °	386.7253	11.20
β-$NaCoPO_4$ (350 ^{0}C)	$P6_5$	a= 10.163938 (15) Å b= 10.163938 (15) Å c= 23.854378 (12) Å	α = 90 ° β = 90 ° γ = 120 °	2134.13	6.67
β-$NaCoPO_4$ (quenched)	$P6_5$	a= 10.167030 (9) Å b= 10.167030 (9) Å c= 23.863644 (6) Å	α = 90 ° β = 90 ° γ = 120 °	2136.25	5.99
α-$NaCoPO_4$	*Pnma*	a= 8.87787 (7) Å b= 6.80082 (6) Å c=5.03085 (4) Å	α = 90 ° β = 90 ° γ = 90 °	304.013	6.23
γ-$NaCoPO_4$	$Pna2_1$	a= 8.25152 (8) Å b= 9.28775 (10) Å c= 4.93135 (6) Å	α = 90 ° β = 90 ° γ = 90 °	378.822	4.95

Table 2.2 (a) Rietveld refined atomic positions for ABW-$NaCoPO_4$

Atoms	Wyckoff positions	Fractional position co-ordinates			Occupancy
		x	y	z	
Na1	4e	0.22359	0.37300	0.01612	1.0000
Co1	4e	0.19623	0.32874	0.50838	1.0000
P1	4e	0.69868	0.40172	0.27901	1.0000
O1	4e	0.41260	0.37059	0.29603	1.0000
O2	4e	0.75060	0.55224	0.28597	1.0000
O3	4e	0.78300	0.35660	0.08752	1.0000
O4	4e	0.84500	0.32740	0.42783	1.0000

Table 2.2 (b) Rietveld refined atomic positions for β-$NaCoPO_4$ (350 ^oC)

Atom	Wyckoff site	x	y	z	Occupancy
Na (Na1)	6a	0.04354	0.03876	0.08986	1.0000
Na (Na2)	6a	0.96458	0.51026	0.08460	1.0000
Na (Na3)	6a	0.53192	0.05015	0.08576	1.0000
Na (Na4)	6a	0.56110	0.50037	0.08216	1.0000
Co (Co1)	6a	0.34180	0.66776	0.15051	1.0000
Co (Co2)	6a	0.69059	0.85506	0.01561	1.0000
Co (Co3)	6a	0.20711	0.37913	0.04186	1.0000
Co (Co4)	6a	0.18155	0.87562	0.01128	1.0000
P (P1)	6a	0.32790	0.68760	0.01435	1.0000
P (P2)	6a	0.68950	0.83640	0.14593	1.0000
P (P3)	6a	0.21610	0.34840	0.17330	1.0000
P (P4)	6a	0.21180	0.88200	0.14400	1.0000
O (O1)	6a	0.71630	0.20370	0.02540	1.0000
O (O2)	6a	0.62980	0.26520	0.90740	1.0000
O (O3)	6a	0.26720	0.81370	0.84710	1.0000
O (O4)	6a	0.66810	0.14750	0.67160	1.0000
O (O5)	6a	0.70420	0.99360	0.13610	1.0000
O (O6)	6a	0.05760	0.20660	0.16850	1.0000
O (O7)	6a	0.23830	0.91740	0.75600	1.0000
O (O8)	6a	0.48260	0.83230	0.01340	1.0000
O (O9)	6a	0.67850	0.99120	0.88390	1.0000
O (O10)	6a	0.55070	0.21990	0.15540	1.0000
O (O11)	6a	0.19570	0.18850	0.01300	1.0000
O (O12)	6a	0.61590	0.91520	0.78270	1.0000
O (O13)	6a	0.26980	0.95360	0.08680	1.0000
O (O14)	6a	0.97190	0.83310	0.01070	1.0000
O (O15)	6a	0.32650	0.05950	0.96960	1.0000
O (O16)	6a	0.21640	0.72050	0.98210	1.0000

Table 2.2 (c) Rietveld refined atomic positions for β-$NaCoPO_4$ quenched at 750 ^oC)

Atom	Wyckoff site	x	y	z	Occupancy
Na (Na1)	6a	0.05801	0.04020	0.09629	1.0000
Na (Na2)	6a	0.95886	0.50596	0.09162	1.0000
Na (Na3)	6a	0.53335	0.05057	0.08953	1.0000
Na (Na4)	6a	0.55712	0.50382	0.08353	1.0000
Co (Co1)	6a	0.33806	0.66599	0.14990	1.0000
Co (Co2)	6a	0.69422	0.85749	0.01530	1.0000
Co (Co3)	6a	0.20507	0.37778	0.04130	1.0000
Co (Co4)	6a	0.17790	0.87117	0.01078	1.0000
P (P1)	6a	0.32790	0.68760	0.01435	1.0000
P (P2)	6a	0.68950	0.83640	0.14593	1.0000
P (P3)	6a	0.21610	0.34840	0.17330	1.0000
P (P4)	6a	0.21180	0.88200	0.14400	1.0000
O (O1)	6a	0.71630	0.20370	0.02540	1.0000
O (O2)	6a	0.62980	0.26520	0.90740	1.0000
O (O3)	6a	0.26720	0.81370	0.84710	1.0000
O (O4)	6a	0.66810	0.14750	0.67160	1.0000
O (O5)	6a	0.70420	0.99360	0.13610	1.0000
O (O6)	6a	0.05760	0.20660	0.16850	1.0000
O (O7)	6a	0.23830	0.91740	0.75600	1.0000
O (O8)	6a	0.48260	0.83230	0.01340	1.0000
O (O9)	6a	0.67850	0.99120	0.88390	1.0000
O (O10)	6a	0.55070	0.21990	0.15540	1.0000
O (O11)	6a	0.19570	0.18850	0.01300	1.0000
O (O12)	6a	0.61590	0.91520	0.78270	1.0000
O (O13)	6a	0.26980	0.95360	0.08680	1.0000
O (O14)	6a	0.97190	0.83310	0.01070	1.0000
O (O15)	6a	0.32650	0.05950	0.96960	1.0000
O (O16)	6a	0.21640	0.72050	0.98210	1.0000

Table 2.2 (d) Rietveld refined atomic positions for α-$NaCoPO_4$

Atom	Wyckoff site	x	y	z	Occupancy
Na1	4c	0.84960(20)	0.2500	0.5333(5)	0.5000
Co1	4a	0.5000	0.5000	0.5000	0.5000
P1	4c	0.1776	0.2500	0.4621	0.5000
O1	4c	0.118	0.2500	0.7495	0.5000
O2	4c	0.353	0.2500	0.4516	0.5000
O3	8d	0.1231	0.0661	0.3165	1.0000

Table 2.2 (e) Rietveld refined atomic positions for γ-$NaCoPO_4$

Atom	Wyckoff site	x	y	z	Occupancy
Co1	4a	0.15171(12)	0.04838(5)	0.9946(5)	1.0000
Na1	4a	-0.0261(4)	0.32110(20)	0.4451(6)	1.0000
P1	4a	0.29019(10)	0.37319(10)	0.05019(10)	1.0000
O1	4a	0.25399(10)	0.20899(10)	0.12299(10)	1.0000
O2	4a	0.44769(10)	0.41069(10)	0.16869(10)	1.0000
O3	4a	0.17131(10)	0.46731(10)	0.18031(10)	1.0000
O4	4a	0.29293(10)	0.39493(10)	0.74593(10)	1.0000

Table 2.3 (a): Selected bond-lengths and BVS calculations for ABW-$NaCoPO_4$

Atom	C.N	Selected Bond Lengths (Å)	BVS
Na^{1+} (1)	6	(Na1) - (O1) : 2.2894(6) (Na1) - (O2) : 2.3573(6) (Na1) - (O3) : 2.3708(6) (Na1) - (O3) : 2.9769(7) (Na1) - (O3) : 2.8122(8) (Na1) - (O4) : 2.2029(6)	1.154 (2)
Co^{2+} (1)	4	(Co1) - (O1) : 1.9812(5) (Co1) - (O2) : 1.9494(4) (Co1) - (O3) : 1.9965(5) (Co1) - (O4) : 1.9297(5)	1.922 (1)

Table 2.3 (b): Selected bond-lengths and BVS calculations for β-$NaCoPO_4$ (350 ^oC)

Atom	C.N	Selected Bond Lengths (Å)	BVS
Na^{1+} (1)	7	(Na1) - (O6) : 2.4911(0) (Na1) - (O6) : 2.9412(0) (Na1) - (O11) : 2.3908(0) (Na1) - (O11) : 2.7689(0) (Na1) - (O13) : 2.8344(0) (Na1) - (O14) : 2.6350(0) (Na1) - (O14) : 2.8860(0)	0.7
Na^{1+} (2)	6	(Na2) - (O2) : 2.6703(0) (Na2) - (O3) : 2.4305(0) (Na2) - (O8) : 2.7318(0) (Na2) - (O9) : 2.3038(0) (Na2) - (O15) : 2.3218(0) (Na2) - (O16) : 2.8889(0)	0.918
Na^{1+} (3)	6	(Na3) - (O1) : 2.2575(0) (Na3) - (O4) : 2.8771(0) (Na3) - (O5) : 2.4176(0) (Na3) - (O8) : 2.6502(0) (Na3) - (O10) : 2.3331(0) (Na3) - (O13) : 2.3339(0)	1.16
Na^{1+} (4)	5	(Na4) - (O3) : 2.8757(0) (Na4) - (O4) : 2.3650(0) (Na4) - (O7) : 2.3102(0) (Na4) - (O12) : 2.4465(0) (Na4) - (O16) : 2.2559(0)	0.998
Co^{2+} (1)	4	(Co1) - (O1) : 1.9340(0) (Co1) - (O2) : 1.9451(0) (Co1) - (O3) : 1.9748(0) (Co1) - (O4) : 1.9945(0)	1.932
Co^{2+} (2)	4	(Co2) - (O5) : 1.9793(0) (Co2) - (O6) : 1.9099(0) (Co2) - (O7) : 1.9738(0) (Co2) - (O8) : 2.0090(0)	1.906
Co^{2+} (3)	4	(Co3) - (O2) : 2.4871(0) (Co3) - (O9) : 1.9578(0) (Co3) - (O10) : 2.0088(0) (Co3) - (O11) : 2.0042(0) (Co3) - (O12) : 1.9909(0)	1.905
Co^{4+} (4)	4	(Co4) - (O13) : 1.9918(0) (Co4) - (O14) : 1.9511(0) (Co4) - (O15) : 1.9745(0) (Co4) - (O16) : 1.9116(0)	1.96

Table 2.3(c): Selected bond-lengths and BVS calculations for β-$NaCoPO_4$ (quenched 750 ^oC)

Atom	C.N	Selected Bond Lengths (Å)	BVS
Na^{1+} (1)	6	(Na1) - (O6) : 2.4164(0) (Na1) - (O11) : 2.4644(0) (Na1) - (O11) : 2.5672(0) (Na1) - (O13) : 2.7127(0) (Na1) - (O14) : 2.7438(0) (Na1) - (O14) : 2.8501(0)	0.708
Na^{1+} (2)	6	(Na2) - (O2) : 2.7403(0) (Na2) - (O3) : 2.5315(0) (Na2) - (O8) : 2.5672(0) (Na2) - (O9) : 2.3611(0) (Na2) - (O15) : 2.2691(0) (Na2) - (O16) : 2.7726(0)	0.924
Na^{1+} (3)	6	(Na3) - (O1) : 2.3087(0) (Na3) - (O4) : 2.8216(0) (Na3) - (O5) : 2.3652(0) (Na3) - (O8) : 2.7105(0) (Na3) - (O10) : 2.2721(0) (Na3) - (O13) : 2.3483(0)	1.134
Na^{1+} (4)	6	(Na4) - (O2) : 2.8376(0) (Na4) - (O3) : 2.9382(0) (Na4) - (O4) : 2.4118(0) (Na4) - (O7) : 2.2759(0) (Na4) - (O12) : 2.4008(0) (Na4) - (O16) : 2.2756(0)	0.996
Co^{2+} (1)	4	(Co1) - (O1) : 1.9223(0) (Co1) - (O2) : 1.9210(0) (Co1) - (O3) : 2.0109(0) (Co1) - (O4) : 1.9967(0)	1.936
Co^{2+} (2)	4	(Co2) - (O5) : 1.9785(0) (Co2) - (O6) : 1.8816(0) (Co2) - (O7) : 1.9859(0) (Co2) - (O8) : 2.0361(0)	1.907
Co^{2+} (3)	4	(Co3) - (O9) : 1.9432(0) (Co3) - (O10) : 2.0128(0) (Co3) - (O11) : 1.9963(0) (Co3) - (O12) : 2.0103(0)	1.903
Co^{2+} (4)	4	(Co4) - (O13) : 2.0208 (0) (Co4) - (O14) : 1.9302(0) (Co4) - (O15) : 2.0054(0) (Co4) - (O16) : 1.8889(0)	1.953

Table 2.3 (d): Selected bond-lengths and BVS calculations for α-$NaCoPO_4$

Atom	C.N	Selected Bond Lengths (Å)	BVS
Na^{1+} (1)	10	(Na1) - (O1) : 2.6193 (19) (Na1) - (O1) : 2.3282 (20) (Na1) - (O2) : 2.4396 (25) (Na1) - (O2) : 2.5916 (25) (Na1) - (O3) X 2: 2.9410(17) (Na1) - (O3) X 2: 2.9503(19) (Na1) - (O3) X 2: 2.2915 (9)	1.366 (2)
Co^{2+} (1)	6	(Co1) - (O1) X 2: 2.3614 (0) (Co1) - (O2) X 2 : 2.1571(0) (Co1) - (O3) X 3: 1.9829 (0)	1.808 (0)

Table 2.3 (e): Selected bond-lengths and BVS calculations for γ-$NaCoPO_4$

Atom	C.N	Selected Bond Lengths (Å)	BVS
Co^{2+} (1)	5	(Co1) - (O1) : 1.8271(14) (Co1) - (O2) : 2.2115(20) (Co1) - (O2) : 1.9276(16) (Co1) - (O3) : 2.2587(19) (Co1) - (O4) : 1.9431(18)	2.192 (5)
Na^{1+} (1)	6	(Na1) - (O1) : 2.9915(32) (Na1) - (O1) : 2.4277(32) (Na1) - (O2) : 2.5571(24) (Na1) - (O3) : 2.4905(30) (Na1) - (O3) : 2.5774(26) (Na1) - (O4) : 2.9079(27)	0.698 (2)

A global view on the formation mechanism of $NaCoPO_4$ compounds

Based on the analysis on the *in-situ* PXRD patterns, we infer the sequence of the formation of $NaCoPO_4$ polymorphs as ABW-$NaCoPO_4$ to β- $NaCoPO_4$ to α- $NaCoPO_4$ to γ- $NaCoPO_4$ upon heating the precursors from RT to 765 °C. It is interesting to note that despite cobalt present in +2 oxidation state, its coordination environment changes from four to six to five upon the phase transformations which requires breaking and forming new bonds. Thus, these phase transitions are reconstructive in nature. To understand the formation mechanism of the

$NaCoPO_4$ polymorphs, the corresponding topologies [$CoPO_4$] frameworks are compared as follows: in the ABW-,α- and γ- $NaCoPO_4$ structures, the units of $[CoO]_n$ (n=4, 6 & 5 respectively) and PO_4 are aligned in separate columns along *a*-, *b*- and *c*-axis respectively. However, the β phase has the columns of mixed CoO_4 and PO_4 units which are aligned along *c*-axis. Further, in the ABW-,α- and γ- $NaCoPO_4$ structures, sodium, cobalt and phosphorous atoms occupy single crystallographic sites as can be seen from Table 2.2, whereas the same atoms are distributed over multiples crystallographic 6a sites in the β structures. Thus, we can consider that the structure of the β phase is a disordered one in comparison with other polymorphs.

As mentioned earlier, the rapid decomposition of $Co(OH)_2$ precursor lead the formation of the ABW compound which can be considered as kinetically stabilized metastable polymorph. Upon heating above 200 °C, it transforms into β- $NaCoPO_4$ and symmetry also increases from $P2_1/n$ to $P6_5$. This transformation can be viewed as mixing of either PO_4 or CoO_4 columns rotating around the *a*-axis of ABW. As the annealing temperature is raised this disordered β-phase structure undergoes irreversible phase transformation starting at ~420 °C to an ordered α-$NaCoPO_4$ and the corresponding symmetry also increases from $P6_5$ to *Pnma*. Further, as the temperature raised to 700 °C, α–phase reversibly transform into another ordered structure (i.e. γ- $NaCoPO_4$). However, it involves lowering of symmetry, i.e. from *Pnma* to $Pna2_1$ which is a subgroup of the former. Although such transformation is unusual, similar observation was reported on the transformation of α- to β-$AgZnPO_4$.[56]

Another interesting aspect of the phase transformation is the transformation of γ- $NaCoPO_4$ to either β- $NaCoPO_4$ or α- $NaCoPO_4$ depending on the cooling rate as shown in Figure 2.11. With the normal cooling to room temperature it transforms into α- $NaCoPO_4$ which is

thermodynamically most stable phase in the family of compounds. Alternatively, when quenched directly in liquid N_2 the formation of β- $NaCoPO_4$ resulted. Whilst the reversible α↔β transformation is driven by the temperature change, the stabilization of the β-phase upon rapid quenching can be understood via entropy change which results in the disordered structure.

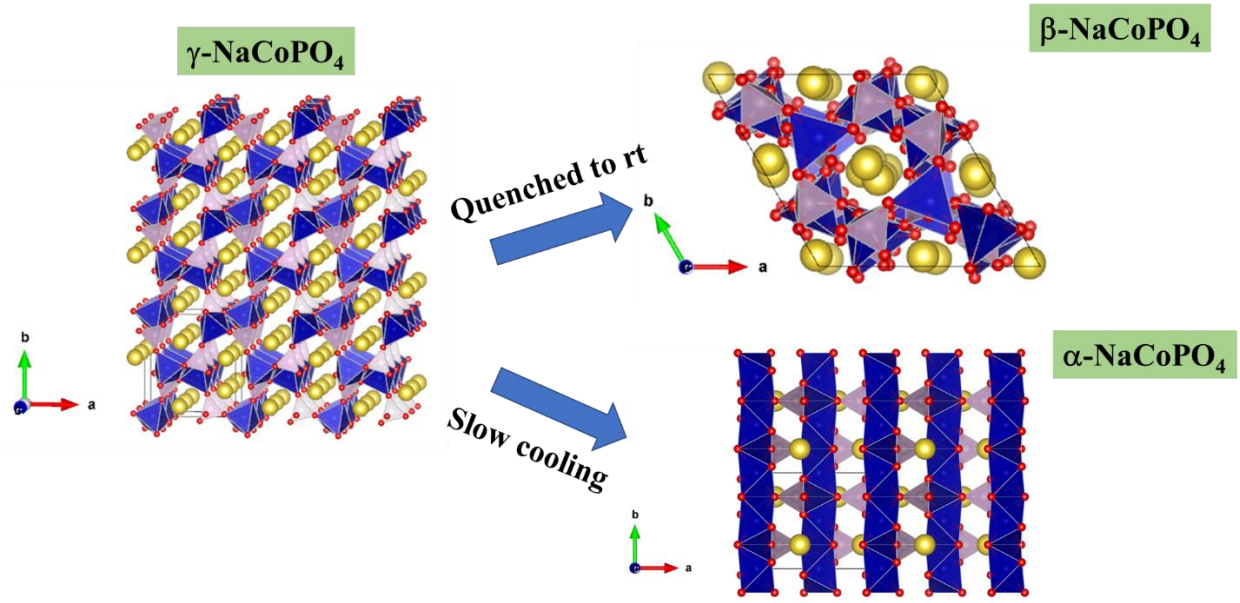

Figure 2.11: Transformation of γ-$NaCoPO_4$ to either β-$NaCoPO_4$ or α-$NaCoPO_4$ depending on the rate of cooling

2.3.3 Theoretical calculations for formation energies

The plots in Figs. 2.12 (a) and (b) show the trends in formation enthalpies of the four phases of $NaCoPO_4$, with respect to elemental constituents and synthetic precursors respectively. The α–phase is found to be most stable while the high-temperature γ–phase is an unstable high-energy state. It is observed that the trend in ΔH_f, with respect to precursors, remains similar to the one computed against elemental constituents.

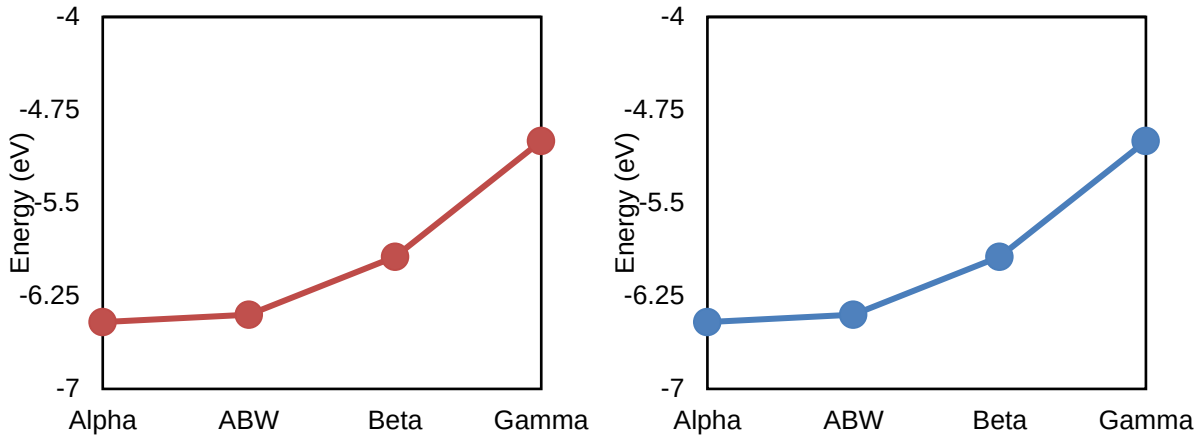

Figure 2.12. Formation Enthalpies of $NaCoPO_4$ phases standardized with respect to a) elemental constituents at standard temperature and pressure, and b) synthetic precursors.

2.3.4 Electrochemical analysis

The electrochemical sodium (de)-intercalation studies of the ABW and β phases were made in Na cells in the voltage window of 4.7 to 2.0 V vs. Na^+/Na^0. It is expected that α-phase is electrochemically inactive as it does not have any feasible channels to extract sodium ions from the structure. The ABW phase showed negligible capacities when tested against sodium metal anode. During the first charge, the β- phase showed a plateau around ~4.2 V vs. Na^+/Na^0 with a capacity of 65 $mAhg^{-1}$, which is equivalent to the removal of 0.37 moles of sodium ions per formula unit (Figure 1.13). Upon subsequent discharge, the voltage profile become more sloppier with an average voltage of 4.0 V vs. Na^+/Na^0 with an intercalation capacity of 22 $mAhg^{-1}$. The poor reversibility could be due to the electrolyte degradation at the high voltages. The limited electrochemical activity could be due to the presence of Co^{2+} in tetrahedra geometry. As the cycling proceeds, the capacity decayed further and reached a value of 14 $mAhg^{-1}$ at the end of 10^{th} cycle. Similar electrochemical responses were earlier reported for red-$NaCoPO_4$.[49]

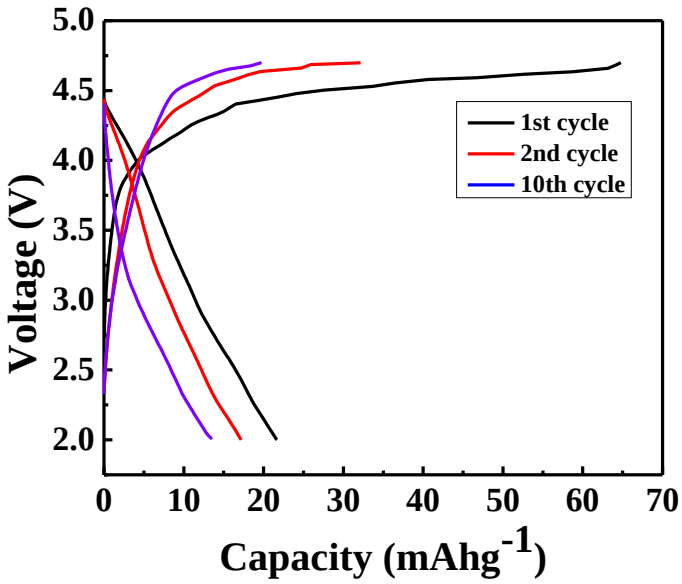

Figure 2.13: Galvanostatic charge-discharge profiles of β-NCPO at C/25 rate; (inset): dQ/dV plot)

2.4 Conclusion:

In summary, we have studied the formation mechanism of the $NaCoPO_4$ family of compounds using two different precursors. While the *in-situ* PXRD studies revealed similar formation mechanism of $NaCoPO_4$ polymorphs for both precursors, the striking difference is noticed for the formation of ABW phase during the annealing of precursor-1. Further the study revealed the presence of new high temperature γ-$NaCoPO_4$ polymorph which reversibly transforms to α phase upon gradual cooling to RT. When quenched the same phase transformed into β-phase. Further, ABW- and β- phases were synthesized and tested in Na cells.

Chapter 3

Chemical Pressure-Stabilized Post Spinel-$NaMnSnO_4$ Cathode for SIBs

3.1 Introduction:

Layered oxides are one of the most extensively studied cathode materials for SIBs. They have comparable specific capacity with respect to Li-based layered cathodes, however, due to their multiple phase transformations during the charge-discharge cycles, their cycle life is limited.[6] One of the major reasons for this structural instability has been attributed to the Jahn-Teller distortion in the transition metal sites. A typical example of it is Na_xMnO_2,wherein Mn is in the degenerate d^{3+} state, which exhibits Jahn-Teller distortion following the reduction of Mn^{4+} to Mn^{3+} and that leads to reduced cyclability.[57]

The transition of layered oxides to spinel compounds have been well documented for systems like Li_xMnO_2 and Li_xCoO_2.[58] In fact, $LiMn_2O_4$ is considered as a promising cathode material for LIBs due to its high voltage (4.0 V), thermal stability, reversible capacity of ~100-120 $mAhg^{-1}$ vs Li^+/Li^0, low cost and abundance of manganese precursors.[31,59,60] $LiMn_2O_4$ (*Fd-3m*) is a mixed valence compound consisting of Mn^{3+} and Mn^{4+} in octahedral geometry. It undergoes a first order transition at 290 K due to Jahn-Teller distortions of Mn^{3+}.[61] It involves partial charge ordering at the octahedral sites. The lithium conduction is through a zig-zag pathway passing through a bottleneck of oxide triangle.[62,63] The electrochemical

displacement of Li with Na was studied for spinel $LiMn_2O_4$ in SIBs.[64] However, after a few cycles, the structure converted into the layered spinel.

On subjecting this spinel to a pressure of 6 GPa, and heating above 1100 °C, post-spinel $Li_{0.92}Mn_2O_4$ was formed which was found to be 6% denser than the former. This compound crystallized into a $CaFe_2O_4$ type structure (*Pnma*) which contain double rutile chains and 1D sodium channels. Theoretical calculations showed that the lithium diffusion barrier for the post-spinel compound is 0.12 eV, which is far less than the spinel compound (0.40 eV).[32] Thus, the kinetics can be expected to be more facile in the post-spinel compound. First principle calculations done on post-spinel AMn_2O_4 (A= Li, Na, Mn) have indicated a higher sodium mobility and structural stability.[65] Post-spinel $NaMn_2O_4$ was first synthesized under high pressure of 4.5 GPa and temperature of 1373 K using stoichiometric mixtures of Na_2O_2 and Mn_2O_3 as starting materials. It was determined to be structurally analogous to $CaFe_2O_4$ (other post-spinel phases are $CaMn_2O_4$ and $CaTi_2O_4$ as shown in Figure 3.1).[66] When tested against sodium metal at 55 °C at a current density of 5 mAg^{-1}, it showed a plateau at 3.0 V vs. Na^+/Na^0 with the specific capacity of 83 $mAhg^{-1}$ in the voltage range of 1.5–4.8 V vs. Na^+/Na^0. Further, it exhibited a capacity retention of 94% at the 200th cycle.[33] This suggests the suppression of Jahn–Teller because of the high barrier of rearranged MnO_6 octahedrons. Therefore, it presents a stable material structure. Nanocrystalline $NaMn_2O_4$ synthesized via high energy mechanical ball milling showed 1st discharge capacity of ~95$mAhg^{-1}$ in the potential window of 2-4.5 V at a rate of 40 mAg^{-1}.[67] Vanadium-based post-spinel $NaV_{1.25}Ti_{0.75}O_4$ has been recently reported by Nazar and co-workers. It gives a reversible capacity ~55 $mAhg^{-1}$ in the voltage range of 1.5-4.5 V at 5mAg^{-1} current density. This material has also been shown as a prospective cathode material for Mg batteries.[68]

In this chapter, we have attempted to synthesize post-spinel manganese oxides without the use of high external pressure. This was achieved by inducing chemical pressure with the substation of large cations, i.e. Sn^{4+}. We could successfully synthesize $NaFeSnO_4$ and $NaMnSnO_4$. $NaFeSnO_4$ has been previously reported for use as an anode material in LIBs with Sn as the active centre.[69]

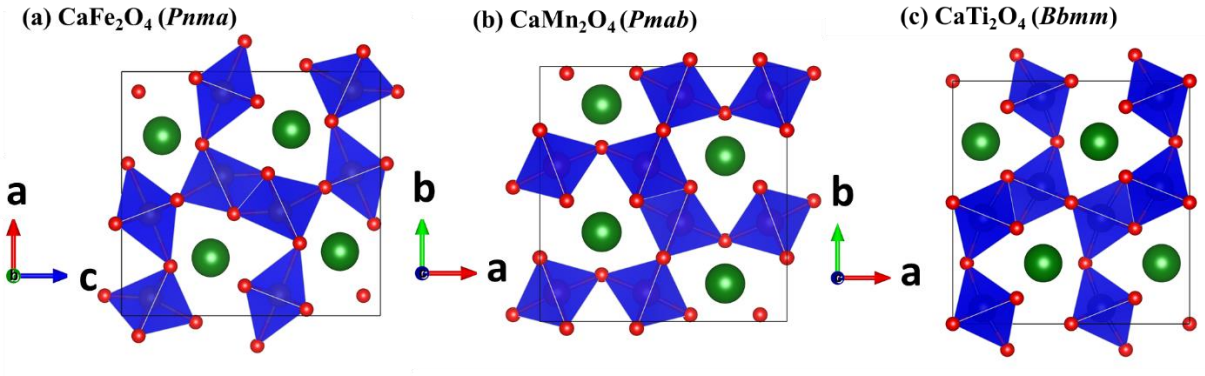

Figure 3.1 Crystal structures of three types of post-spinel compounds. All have distorted MO_6 octahedra forming "double-rutile chains" and cation Ca^{2+} in 8-fold oxygen coordination sphere. $CaFe_2O_4$-type has the transition metal in two 4c sites, while the $CaMn_2O_4$ and $CaTi_2O_4$-type have them in 8e and 8f sites respectively. In CM-phase, all atoms are displaced from the mirror plane while in CF and CT phases, the atoms are located in the mirror plane.

3.2 Experimental section

3.2.1 Synthesis- Na_2CO_3 (Sigma-Aldrich, 99.5%), Mn_2O_3 (Sigma-Aldrich, 99%) and SnO_2 (Alfa-Aesar, 99.9%) were mixed in the stoichiometry of Na:Mn:Sn = 1:1:1 and ball-milled in a SPEX Sample Prep Mixer/Mill 800M for 30 minutes to form the precursor. The precursor was then heated to 1200 ^oC at the rate of 5 $^oC\ min^{-1}$ and subsequently annealed for a day and then slowly cooled (0.5 $^oC\ min^{-1}$) to room temperature to obtain a black-colored powder of $NaMnSnO_4$. It is necessary to cool at a very slow rate so that the system uptakes maximum oxygen. Oxygen deficiency (or presence of small amounts of impurity) in the system leads to rapid degradation into SnO_2 and layered Na_xMnO_2. However, the slowly-cooled synthesized product is stable in air for up to 6 months.

Similarly, $NaFeSnO_4$ was synthesized by annealing a precursor mixture of stoichiometric amounts of Na_2CO_3 (Sigma-Aldrich, 99.5%), Fe_2O_3 (Sigma-Aldrich, 99%) and SnO_2 (Alfa-Aesar, 99.9%) at 900 ^oC for a day and allowing it to cool slowly.

3.2.2 Powder X-ray diffraction- PXRD for the as-synthesized samples were recorded using a Cu Ka (λ=1.5406 Å) radiation on a Bruker D8 diffractometer. Rietveld refinements were performed using FULLPROF software.[39]

3.2.3 Electrode preparation and cell assembly- The electrodes were prepared by ball-milling 70 wt% of $NaFeSnO_4$ (and $NaMnSnO_4$), 22 wt% TIMICAL SUPER C-45 carbon (MTI) and 8 wt% poly(vinylidene fluoride) (Sigma-Aldrich) for 20 minutes and then making a slurry which was coated on a 0.025mm thick carbon-coated aluminum foil current collector. The electrode laminate was dried at 70 ^oC in a vacuum over for overnight and punched as a disk (10 mm diameter). The Swagelok cells were assembled in a dry box (H2O<0.1 and O2<0.1). Sodium metal (Sigma 99.9%) was used as the counter electrode and the electrolyte contained 1.0 M $NaPF_6$ in a mixture of ethylene carbonate (45 wt%), propylene carbonate (45 wt%), dimethyl carbonate (10 wt%) and Fluoroethylene carbonate (2 wt%). For *ex-situ* XRD analysis, the electrodes coated on pin hole free thin aluminum foil (Alfa 99.99%, 10-micron thickness) were used. The electrodes were harvested from the Swagelok cells at different state of charges, washed and dried inside the glove box. Then, the electrodes were mounted on a glass plate upside down in a way which Al foil serve as the window and was hermitically sealed with Kapton tape.

3.2.4 Electrochemical measurements- Galvanostatic Cycling with Potential Limitation **(**GCPL) measurements were taken using Biologic BCS-805. The $NaMnSnO_4$ and $NaFeSnO_4$

electrodes were cycled against sodium metal at current rate of C/25 in between potential range 2.0 - 4.5 V vs Na^+/Na^0.

3.2.5 Field Emission Scanning Electron Microscope (FESEM)- FESEM for $NaMnSnO_4$ was carried out on ZEISS GeminiSEM 500 at a probe current of 20 nA. Energy-dispersive X-ray spectroscopy (EDS) measurements and elemental mapping were also done using the same instrument. FESEM image for $NaFeSnO_4$ was obtained from NOVA NANO SEM 600.

3.3 Results and Discussion

The PXRD patterns of as-synthesized $NaMnSnO_4$ and $NaFeSnO_4$ along with reference pattern of $NaFeSnO_4$ phase are displayed in Figure 3.2.

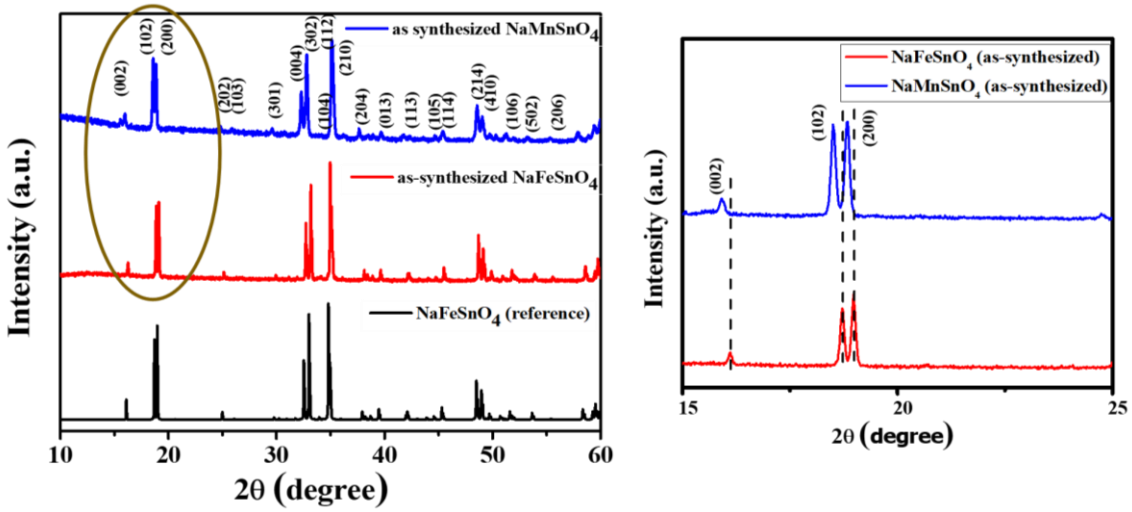

Figure 3.2 XRD patterns of $NaMnSnO_4$ and $NaFeSnO_4$ indexed in the 2θ range of 10° to 60°. The pattern on the right shows the peak shift in the indicated zoomed-in area.

All the reflections of $NaMnSnO_4$ and $NaFeSnO_4$ samples could be fully indexed with *Pnma* space group, thus confirming purity. In comparison with $NaFeSnO_4$, the reflections of the $NaMnSnO_4$ were found to be shifted towards lower 2θ values, thus indicating the expansion of unit cell volume. The calculated cell parameters of $NaMnSnO_4$ and $NaFeSnO_4$ phases are displayed in Table 3.1. It is observed that the values of *a*- and *c*-parameters increase while *b*-

parameter decreases upon replacing Fe^{3+} with Mn^{3+} which could be due to the differences in their ionic radii.

Table 3.1 Comparing of lattice parameters of as-synthesized $NaMnSnO_4$ and $NaFeSnO_4$

System	Space group	Lattice parameters		Volume ($Å^3$)	R_{wp}
$NaMnSnO_4$	*Pnma*	a= 9.42028 (9) Å b= 3.03451 (4) Å c= 11.12908 (13) Å	α = 90 ° β = 90 ° γ = 90 °	318.135444	3.98
$NaFeSnO_4$	*Pnma*	a= 9.33623 (34) Å b= 3.06343 (9) Å c= 10.97868 (37) Å	α = 90 ° β = 90 ° γ = 90 °	315.339734	6.36

To solve the crystal structure of $NaMnSO_4$, Rietveld refinement was carried out based on $NaFeSnO_4$ as model structure. The fitting is shown in Figure 3.3.

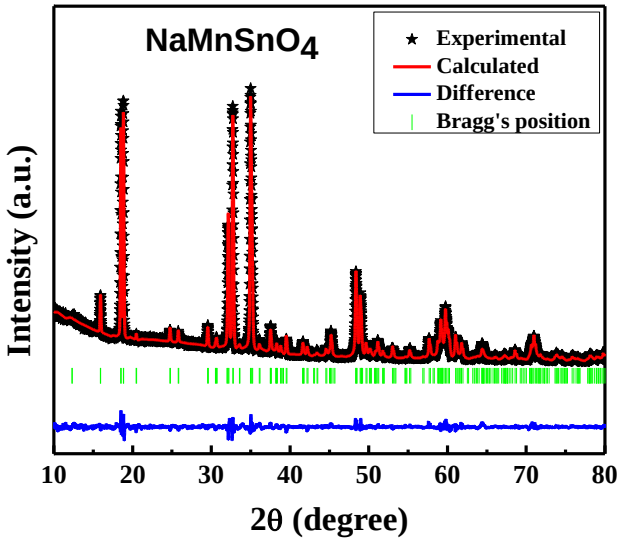

Figure 3.3 (a) Rietveld Refined fitting of $NaMnSnO_4$

The final atomic coordinates, bond distances and Bond Valence Sum (BVS) are displayed in Table 3.2 and 3.3 respectively. The crystal structure of $NaMnSnO_4$ along *b*-direction is shown in Figure 3.4. It consists of double rutile chains of edge-shared $(Mn1/Sn1)O_6$ and

$(Mn2/Sn2)O_6$ octahedra which share corners and edges to make three-dimensional framework. In this network, sodium ion channels are located along *b*-axis.

Table 3.2 Refined atomic positions of $NaMnSnO_4$. The occupancies of all atoms were fixed during refinement.

Atom	Wyckoff Site	x	y	z	Occupancy
Na1	4c	0.2486(6)	0.25000	0.3451(5)	1.0000
Mn1	4c	0.05848(14)	0.25000	0.11664(15)	0.5000
Mn2	4c	0.08676(15)	0.25000	0.60251(13)	0.5000
Sn1	4c	0.05848(14)	0.25000	0.11664(15)	0.5000
Sn2	4c	0.08676(15)	0.25000	0.60251(13)	0.5000
O1	4c	0.2925(8)	0.25000	0.6590(7)	1.0000
O2	4c	0.3707(7)	0.25000	-0.0144(7)	1.0000
O3	4c	0.4642(9)	0.25000	0.2139(7)	1.0000
O4	4c	0.0783(8)	0.25000	-0.0753(5)	1.0000

Table 3.3 Bond Lengths and BVS calculation of $NaMnSnO_4$

Atom	C.N.	Bond Lengths (in Å)	BVS
Na^{1+} (1)	8	(Na1)-(O1) : 2.590(7) (Na1)-(O1) : 2.590(7) (Na1)-(O2) : 2.464(7) (Na1)-(O2) : 2.464(7) (Na1)-(O3) : 2.489(10) (Na1)-(O3) : 2.758(10) (Na1)-(O4) : 2.406(7) (Na1)-(O4) : 2.406(7)	1.197(9)
Mn^{3+} (1)/ Sn^{4+} (1)	6	(Mn1/Sn1)-(O1) : 2.109(6) (Mn1/Sn1)-(O1) : 2.109(6) (Mn1/Sn1)-(O3) : 2.092(8) (Mn1/Sn1)-(O4) : 2.140(6) (Mn1/Sn1)-(O4) : 2.050(6) (Mn1/Sn1)-(O4) : 2.050(6)	Mn1 = 2.456(16) Sn1 = 3.364(23)
Mn^{3+} (1)/ Sn^{4+} (1)	6	(Mn2/Sn2)-(O1) : 2.043(8) (Mn2/Sn2)-(O2) : 2.224(7) (Mn2/Sn2)-(O2) : 2.044(6) (Mn2/Sn2)-(O2) : 2.044(6) (Mn2/Sn2)-(O3) : 2.011(6) (Mn2/Sn2)-(O3) : 2.011(6)	Mn2 = 2.691(18) Sn2 = 3.983(26)

Lower values of BVS for Mn1 and Sn1 may be due to the higher distortion of $(Mn1/Sn1)O_6$ as compared to $(Mn2/Sn2)O_6$. In the $(Mn2/Sn2)O_6$ octahedra, one of the (Mn2/Sn2)-O2 bond has a large elongation which may indicate the presence of a Jahn-Teller center. However, since none of the elongations are observed along both the axial bonds in either of the Mn^{3+} centers, the Jahn Teller distortions are suppressed up to an extent. The cation mixing with Sn^{4+} ($4d^{10}$: Jahn-Teller inactive) at the same Wyckoff sites may also contribute to this suppression. The suppression of Jahn-Teller distortions have been studied for similar materials synthesized under high-pressure.[65] Thus the chemical pressure of Sn acts similarly to external pressure for creating a higher barrier for rearranging of MnO_6 octahedrons.

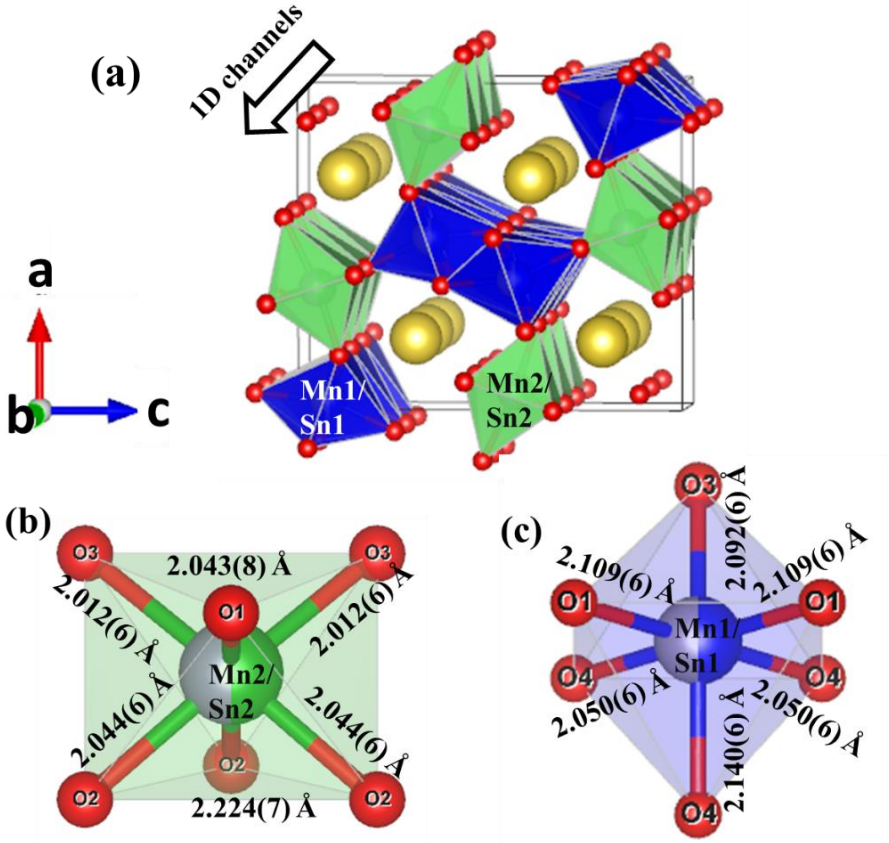

Figure 3.4 (a) Crystal structure of $NaMnSnO_4$ (b) $(Mn2/Sn2)O_6$ and (c) $(Mn1/Sn1)O_6$ octahedra with their corresponding bond lengths (viewed along *a*- direction)

Figure 3.5 (a) and (b) shows the FESEM images of $NaMnSnO_4$ and $NaFeSnO_4$ respectively. Both show an irregular shaped morphology with agglomeration. The average particle size of $NaMnSnO_4$ was found to be 1-2μm while that of $NaFeSnO_4$ was found to be about slightly larger at 4-6μm. This slight difference cannot be used to explain the drastic change in electrochemistry of the two materials as shown in the next section. Figure 3.6 shows the Energy dispersive X-ray analysis (EDAX) spectra of $NaMnSnO_4$. The composition obtained from EDAX was close $NaMnSnO_{2.72}$, though since oxygen is not properly quantifiable using EDAX, this discrepancy can be ignored. We are more interested in the ratio sodium and the metal ions which was found to be 1:1:1.

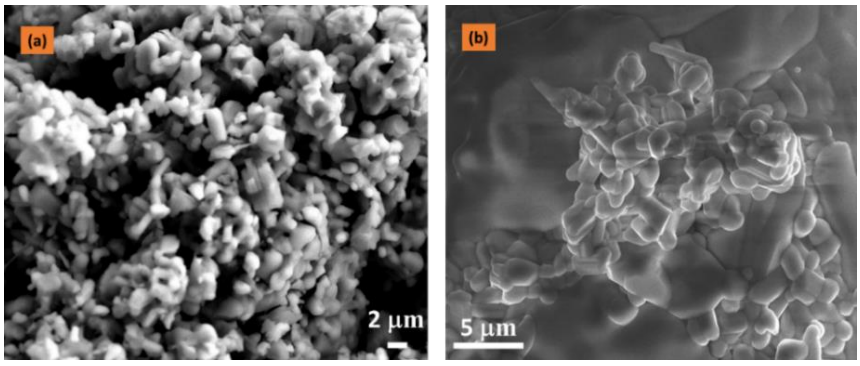

Figure 3.5 FESEM images of (a) $NaMnSnO_4$ and (b) $NaFeSnO_4$

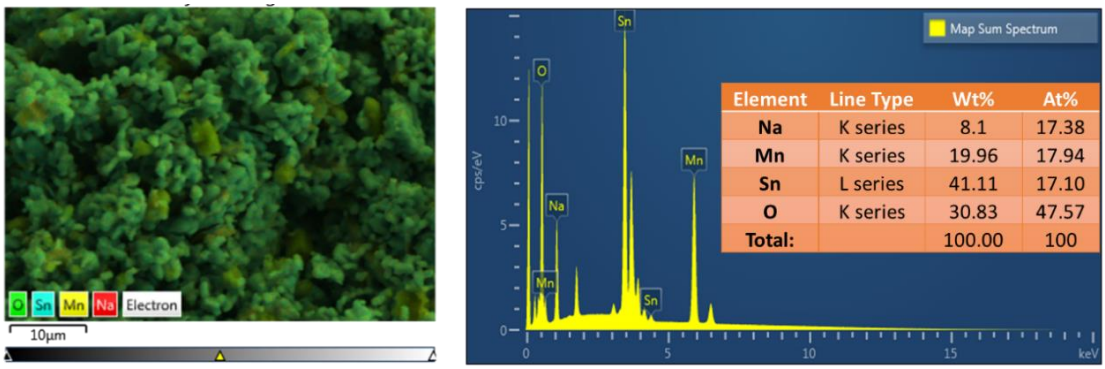

Figure 3.6 EDAX spectra of the selected area of $NaMnSnO_4$ (left) and composition table (inset)

FESEM image and the corresponding elemental mapping of the prepared $NaMnSnO_4$ electrode is given in Figure 3.7. It was observed that the elements are uniformly distributed throughout the electrode surface

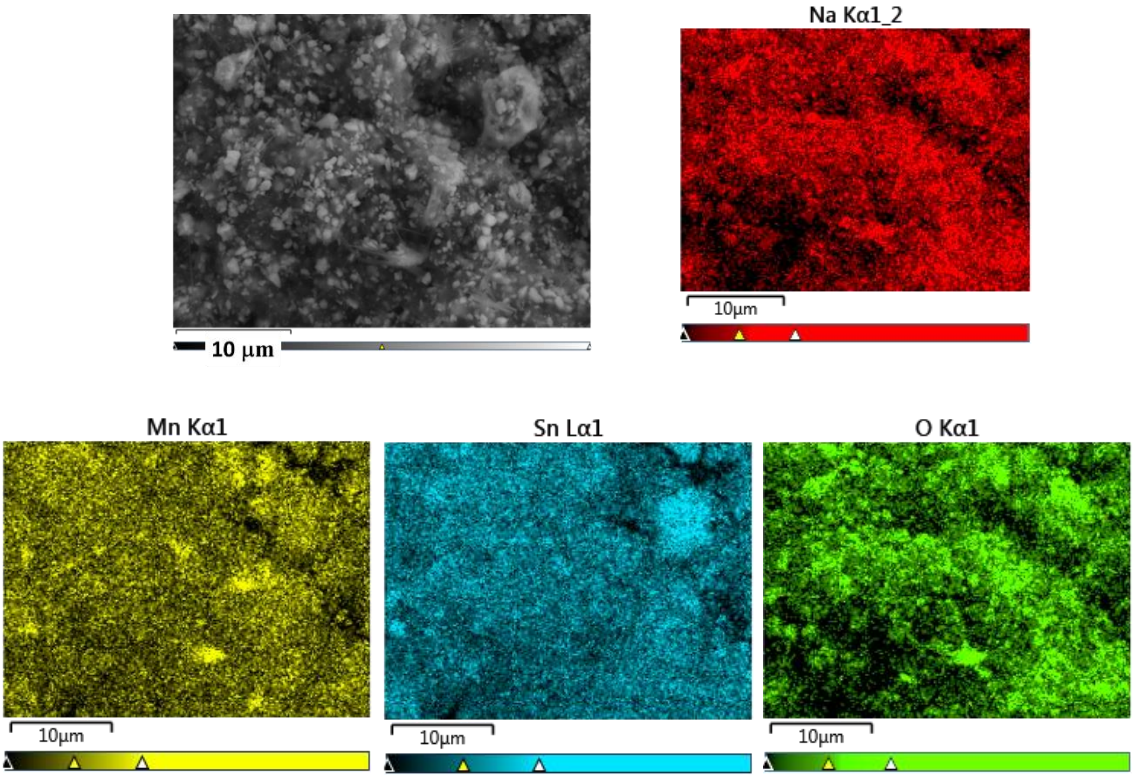

Figure 3.7 Elemental mapping of Na, Mn, Sn and O in the selected area of $NaMnSnO_4$ electrode (top left image)

Electrochemical sodium (de)-intercalation studies of $NaFeSnO_4$ and $NaMnSnO_4$ were performed against sodium metal at C/25 in the voltage window of 4.5-2.0 V vs. Na^+/Na^0 (Figure 3.8 (a) and 3.8 (b) respectively). The theoretical capacity for both the systems is calculated to be ~112 $mAhg^{-1}$. The $NaFeSnO_4$ exhibited barely legible reversible capacity (5 $mAhg^{-1}$) which could be due to the inaccessibility of the Fe^{3+}/Fe^{4+} redox couple. It can also be seen from dQ/dV graph (Figure 3.8 (b) inset) which does not show the presence of any redox reaction. During the first charge, the voltage profile of $NaMnSnO_4$ rise smoothly to 4.5 V vs. Na^+/Na^0 with a charge capacity of ~ 35 $mAhg^{-1}$ which is equivalent to the removal of

0.31 moles of sodium ions. Upon the subsequent discharge, the voltage of $NaMnSnO_4$ cathode decreased to 2.0 V with a reversible capacity of 28 $mAhg^{-1}$. The corresponding redox activity could be tentatively ascribed to the operation of $Mn^{4+/3+}$ couple. The multiple redox features present in the dQ/dV profiles could due to formation of multiple phase during charge and discharge process.

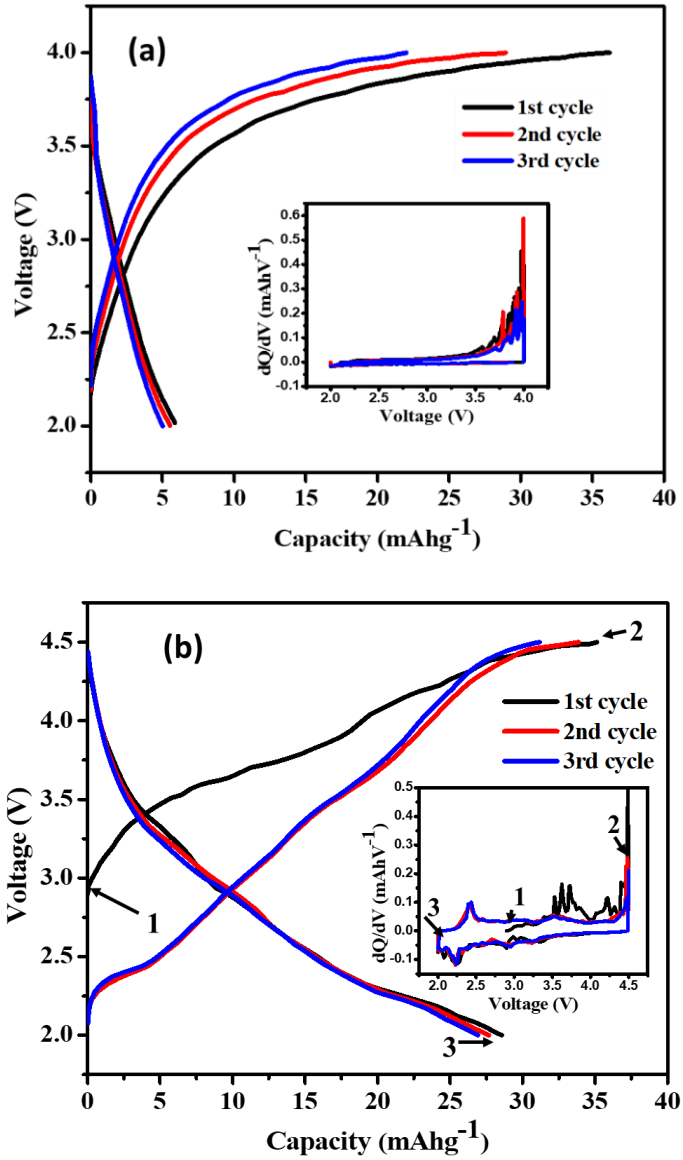

Figure 3.8 Galvanostatic charge-discharge profiles of (a)$NaFeSnO_4$ (b)$NaMnSnO_4$ for the first three cycles at C/25 rate. The inset within each graph shows its corresponding dQ/dV plot.

To understand the electrochemical (de)-intercalation mechanism of $NaMnSnO_4$, *ex-situ* XRD patterns are collected at the end of first charge (4.5 V vs. Na^+/Na^0) and discharge (2.0 V vs. Na^+/Na^0). The collected patterns do not show any significant changes in comparison with the pristine electrode, which indicates the robustness of the crystal structure during sodium (de)-intercalation (Figure 3.9).

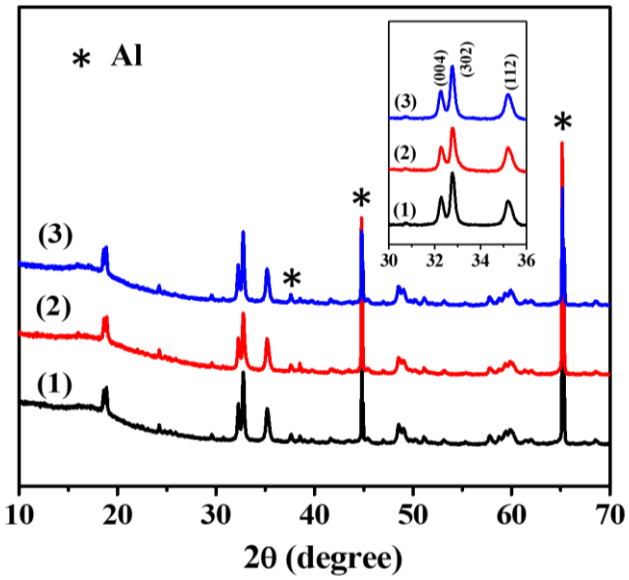

Figure 3.9 *ex-situ* XRD patterns at select potentials (marked in Figure 3.8 (b)) during electrochemical cycling.

3.4 Conclusion:

To sum up, we have shown that the formation of post-spinel oxides is possible even without external high pressures by inculcating a chemically driven pressure within the structure. This led us to successfully synthesize $CaFe_2O_4$-type $NaMnSnO_4$ at ambient pressure. This material has been studied as a cathode in SIBs. The capacity attained is low (~30 $mAhg^{-1}$) and needs to be improved, but the high structural stability and suppressed Jahn-Teller distortion instigates further investigations of these post-spinel compounds as prospective cathode materials for SIBs.

REFERENCES

(1) *World Energy Outlook*; **2015**; Vol. 23.

(2) World Health Organization - WHO Global Ambient Air Quality Database, **2018**.

(3) Hwang, J. Y.; Myung, S. T.; Sun, Y. K. Sodium-Ion Batteries: Present and Future. *Chem. Soc. Rev.* **2017**, *46* (12), 3529-3614.

(4) Slater, M. D.; Kim, D.; Lee, E.; Johnson, C. S. Sodium-Ion Batteries. *Adv. Funct. Mater.* **2013**, *23* (8), 947–958.

(5) Tang, J.; Dysart, A. D.; Pol, V. G. Advancement in Sodium-Ion Rechargeable Batteries. *Curr. Opin. Chem. Eng.* **2015**, *9*, 34–41.

(6) Nayak, P. K.; Yang, L.; Brehm, W.; Adelhelm, P. From Lithium-Ion to Sodium-Ion Batteries: Advantages, Challenges, and Surprises. *Angew. Chem. Int. Ed.* **2018**, *57* (1), 102–120.

(7) Goodenough, J. B.; Park, K. S. The Li-Ion Rechargeable Battery: A Perspective. *J. Am. Chem. Soc.* **2013**, *135* (4), 1167–1176.

(8) Lung-Hao Hu, B.; Wu, F. Y.; Lin, C. Te; Khlobystov, A. N.; Li, L. J. Graphene-Modified $LiFePO_4$ Cathode for Lithium Ion Battery beyond Theoretical Capacity. *Nat. Commun.* **2013**, *4*, 1687.

(9) Liu, C.; Neale, Z. G.; Cao, G. Understanding Electrochemical Potentials of Cathode Materials in Rechargeable Batteries. *Mater. Today* **2016**, *19* (2), 109–123.

(10) Jacob, J. The Chalkboard: C Rating of Batteries: A Misleading Concept, C Flux Rather than C Rate. *Electrochem. Soc. Interface* **2018**, *27* (2), 42–43.

(11) Masquelier, C.; Croguennec, L. Polyanionic (Phosphates, Silicates, Sulfates) Frameworks as Electrode Materials for Rechargeable Li (or Na) Batteries. *Chem. Rev.*

2013, *113* (8), 6552–6591.

(12) Zhou, W.; Xue, L.; Lü, X.; Gao, H.; Li, Y.; Xin, S.; Fu, G.; Cui, Z.; Zhu, Y.; Goodenough, J. B. $Na_xMV(PO_4)_3$ (M = Mn, Fe, Ni) Structure and Properties for Sodium Extraction. *Nano Lett.* **2016**, *16* (12), 7836–7841.

(13) Wang, Q. C.; Meng, J. K.; Yue, X. Y.; Qiu, Q. Q.; Song, Y.; Wu, X. J.; Fu, Z. W.; Xia, Y. Y.; Shadike, Z.; Wu, J.; et al. Tuning P2-Structured Cathode Material by Na-Site Mg Substitution for Na-Ion Batteries. *J. Am. Chem. Soc.* **2019**, *141* (2), 840–848.

(14) Gao, R.; Hu, Z.; Sun, L.; Wang, H.; Li, Z.; Liu, X. Different Effects of Al Substitution for Mn or Fe on the Structure and Electrochemical Properties of $Na_{0.67}Mn_{0.5}Fe_{0.5}O_2$ as a Sodium Ion Battery Cathode Material . *Inorg. Chem.* **2018**, *57* (9), 5249–5257.

(15) Zhou, H.; Ryan Tian, Z.; Ang, S. S. Improving the Cycling Stability of $Na_3V_2(PO_4)_3$ Nanoparticle in Aqueous Sodium Ion Batteries by Introducing Carbon Support. *Mater. Renew. Sustain. Energy* **2016**, *5* (1).

(16) Kim, J.; Okubo, M.; Kudo, T.; Kojima, N.; Honma, I.; Enomoto, M.; Hosono, E.; Zhou, H. Nanosize Effect on High-Rate Li-Ion Intercalation in $LiCoO_2$ Electrode . *J. Am. Chem. Soc.* **2007**, *129* (23), 7444–7452.

(17) Wang, P. F.; You, Y.; Yin, Y. X.; Guo, Y. G. Layered Oxide Cathodes for Sodium-Ion Batteries: Phase Transition, Air Stability, and Performance. *Adv. Energy Mater.* **2018**, *8* (8), 1–23.

(18) Gond, R.; Sada, K.; Senthilkumar, B.; Barpanda, P. Bifunctional Electrocatalytic Behavior of Sodium Cobalt Phosphates in Alkaline Solution. *Chem. Electro. Chem.* **2018**, *5* (1), 153–158.

(19) Berthelot, R.; Carlier, D.; Delmas, C. Electrochemical Investigation of the P2–Na_xCoO_2 Phase Diagram. *Nat. Mater.* **2010**, *10* (1), 74–80.

(20) Han, M. H.; Gonzalo, E.; Singh, G.; Rojo, T. A Comprehensive Review of Sodium Layered Oxides: Powerful Cathodes for Na-Ion Batteries. *Energy Environ. Sci.* **2015**, *8* (1), 81–102.

(21) De La Llave, E.; Borgel, V.; Park, K. J.; Hwang, J. Y.; Sun, Y. K.; Hartmann, P.; Chesneau, F. F.; Aurbach, D. Comparison between Na-Ion and Li-Ion Cells: Understanding the Critical Role of the Cathodes Stability and the Anodes Pretreatment on the Cells Behavior. *ACS Appl. Mater. Interfaces* **2016**, *8* (3), 1867–1875.

(22) Sathiya, M.; Hemalatha, K.; Ramesha, K.; Prakash, A. S. Synthesis , Structure , and Electrochemical Properties of the Layered Sodium Insertion Cathode. *Chem. Mater.* **2012**, *24* (10), 1846–1853

(23) A.K. Padhi, K. S. N. and J. B. G. Phospho-Olivines as Positive-ELectrode Materials for Rechargeable Lithium Batteries. *J. Electrochem. Soc.* **1997**, *144* (4), 1188–1194.

(24) Zhao, L.; Zhou, D.; Huang, W.; Kang, X.; Shi, Q.; Deng, Z.; Yan, X.; Yu, Y. Electrochemical Performances of Maricite $NaFePO_4$/C as Cathode Material for Sodium-ion and Lithium-ion Batteries. *Int. J. Electrochem. Sci.* **2017**, *12* (4), 3153–3165.

(25) Fang, Y.; Liu, Q.; Xiao, L.; Ai, X.; Yang, H.; Cao, Y. High-Performance Olivine NaFePO4 Microsphere Cathode Synthesized by Aqueous Electrochemical Displacement Method for Sodium-ion Batteries. *ACS Appl. Mater. Interfaces* **2015**, *7* (32), 17977–17984.

(26) D. B. Porter , R. Olazcuaga , C. Delmas , F. Cherkaoui, R. Brochu and G. L. Flem,

Rev. Chim. Miner., **1980**, *17*, 458–465.

(27) Song, W.; Ji, X.; Wu, Z.; Zhu, Y.; Yang, Y.; Chen, J.; Jing, M.; Li, F.; Banks, C. E. First Exploration of Na-Ion Migration Pathways in the NASICON Structure $Na_3V_2(PO_4)_3$. *J. Mater. Chem. A* **2014**, *2* (15), 5358–5362.

(28) Shakoor, R. A.; Seo, D. H.; Kim, H.; Park, Y. U.; Kim, J.; Kim, S. W.; Gwon, H.; Lee, S.; Kang, K. A Combined First Principles and Experimental Study on $Na_3V_2(PO_4)_2F_3$ for Rechargeable Na Batteries. *J. Mater. Chem.* **2012**, *22* (38), 20535–20541.

(29) Barpanda, P.; Ye, T.; Nishimura, S. I.; Chung, S. C.; Yamada, Y.; Okubo, M.; Zhou, H.; Yamada, A. Sodium Iron Pyrophosphate: A Novel 3.0 V Iron-Based Cathode for Sodium-Ion Batteries. *Electrochem. Commun.* **2012**, *24* (1), 116–119.

(30) Nose, M.; Nakayama, H.; Nobuhara, K.; Yamaguchi, H.; Nakanishi, S.; Iba, H. $Na_4Co_3(PO_4)_2P_2O_7$: A Novel Storage Material for Sodium-Ion Batteries. *J. Power Sources* **2013**, *234*, 175–179.

(31) Cui, Y.; Chan, C. K.; Kim, D. K.; Yang, Y.; Huggins, R. A.; Ruffo, R.; Muralidharan, P.; Lee, H.-W.; Peng, H. Spinel $LiMn_2O_4$ Nanorods as Lithium Ion Battery Cathodes . *Nano Lett.* **2008**, *8* (11), 3948–3952.

(32) Zhang, L.; Takada, K.; Nagai, T.; Huang, Q.; Yamaura, K.; Takayama-Muromachi, E.; Baba, Y.; Kosuda, K.; Matsui, Y. Spinel-to-$CaFe_2O_4$ -Type Structural Transformation in $LiMn_2O_4$ under High Pressure . *J. Am. Chem. Soc.* **2006**, *128* (29), 9448–9456.

(33) Liu, X.; Wang, X.; Iyo, A.; Yu, H.; Li, D.; Zhou, H. High Stable Post-Spinel $NaMn_2O_4$ Cathode of Sodium Ion Battery. *J. Mater. Chem. A* **2014**, *2* (36), 14822–14826.

(34) Bard, A. J.; Faulkner, L. R. *Electrochemical Methods, Fundamentals and*

Applications; **2001**; Vol. 2nd Edition.

(35) BT-Lab Software:Techniques and Applications, **2014**.

(36) Bragg, W. L. The Diffraction of Short Electromagnetic Waves by a Crystal. *Scientia* **1929**, *23* (45), 153.

(37) Rietveld, H. M. A Profile Refinement Method for Nuclear and Magnetic Structures. *J. Appl. Crystallogr.* **1969**, *2*, 65–71.

(38) Toby, B. H. EXPGUI, a Graphical User Interface for GSAS. *J. Appl. Crystallogr.* **2001**, *34* (2), 210–213.

(39) Rodriguez-Carvajal, J. FULLPROF: A Program for Rietveld Refinement and Pattern Matching Analysis. *Satellite meeting on powder diffraction of the XV congress of the IUCr*; **1990**; *127*.

(40) Toby, B. H. R Factors in Rietveld Analysis: How Good Is Good Enough? *Powder Diffr.* **2008**, *21* (01), 67–70.

(41) Hwang, J. Y.; Myung, S. T.; Sun, Y. K. Sodium-Ion Batteries: Present and Future. *Chem. Soc. Rev.* **2017**, *46* (12), 3529–3614.

(42) Palomares, V.; Serras, P.; Villaluenga, I.; Hueso, K. B.; Carretero-González, J.; Rojo, T. Na-Ion Batteries, Recent Advances and Present Challenges to Become Low Cost Energy Storage Systems. *Energy Environ. Sci.* **2012**, *5* (3), 5884–5901.

(43) Zhu, Y.; Xu, Y.; Liu, Y.; Luo, C.; Wang, C. Comparison of Electrochemical Performances of Olivine $NaFePO_4$ in Sodium-Ion Batteries and Olivine $LiFePO_4$ in Lithium-Ion Batteries. *Nanoscale* **2013**, *5* (2), 780–787.

(44) Senthilkumar, B.; Sankar, K. V.; Vasylechko, L.; Lee, Y. S.; Selvan, R. K. Synthesis and Electrochemical Performances of Maricite-$NaMPO_4$ (M = Ni, Co, Mn) Electrodes

for Hybrid Supercapacitors. *RSC Adv.* **2014**, *4* (95), 53192–53200.

(45) Hammond, R.; Barbier, J. Structural Chemistry of $NaCoPO_4$. *Acta Crystallogr. Sect. B Struct. Sci.* **1996**, *52* (3), 440–449.

(46) Le, S. N.; Eng, H. W.; Navrotsky, A. Energetics of Cobalt Phosphate Frameworks: α, β, and Red $NaCoPO_4$. *J. Solid State Chem.* **2006**, *179* (12), 3731–3738.

(47) Feng, P.; Bu, X.; Tolbert, S. H.; Stucky, G. D. Syntheses and Characterizations of Chiral Tetrahedral Cobalt Phosphates with Zeolite ABW and Related Frameworks. *J. Am. Chem. Soc.* **1997**, *119* (10), 2497–2504.

(48) Feng, P.; Bu, X.; Stucky, G. D. Synthesis, Crystal Structure, and Magnetic Properties of a New Polymorphic Sodium Cobalt Phosphate with Trigonal Bipyramidal Co^{2+} and a Tunnel Structure. *J. Solid State Chem.* **1997**, *129* (2), 328–333.

(49) Gutierrez, A.; Kim, S.; Fister, T. T.; Johnson, C. S. Microwave-Assisted Synthesis of $NaCoPO_4$ Red-Phase and Initial Characterization as High Voltage Cathode for Sodium-Ion Batteries. *ACS Appl. Mater. Interfaces* **2017**, *9* (5), 4391–4396.

(50) Kimura, K.; Kimura, T. Magnetoelectricity in the Structurally Chiral and Polar Antiferromagnet β-$NaCoPO_4$. *J. Phys. Soc. Japan* **2015**, *84* (3), 1–5.

(51) Kim, H.; Park, J.; Park, I.; Jin, K.; Jerng, S. E.; Kim, S. H.; Nam, K. T.; Kang, K. Coordination Tuning of Cobalt Phosphates towards Efficient Water Oxidation Catalyst. *Nat. Commun.* **2015**, *6*, 1–11.

(52) Bianchini, F.; Fjellvåg, H.; Vajeeston, P. A First-Principle Study of $NaMPO_4$ (M = Mn, Fe, Co, Ni) Possible Novel Structures as Cathode Materials for Sodium-Ion Batteries: Structural and Electrochemical Characterisation. *Mater. Chem. Phys.* **2018**, *219*, 212–221.

(53) Yim, W. M.; Paff, R. J. Thermal Expansion of AlN, Sapphire, and Silicon. *J. Appl. Phys.* **1974**, *45* (3), 1456–1457.

(54) Fischer, P.; Lujàn, M.; Kubel, F.; Schmid, H. Crystal Structure and Magnetic Ordering in Magnetoelectric $KNiPO_4$ Investigated by Means of X-Ray and Neutron Diffraction. *Ferroelectrics* **1994**, *162* (1), 37–44.

(55) Blum, D.; Durif, A.; Averbuch-pouchot, M. T. Crystal Structures of the Three Forms of $CsZnPO_4$. *Ferroelectrics* **1986**, *69* (1), 283–292.

(56) Hammond, R.; Barbier, J.; Gallardo, C. Crystal Structures and Crystal Chemistry of $AgXPO_4$ (X=Be, Zn). *J. Solid State Chem.* **1998**, *141* (1), 177–185.

(57) Kim, S.; Ma, X.; Ong, S. P.; Ceder, G. A Comparison of Destabilization Mechanisms of the Layered Na_XMO_2 and Li_XMO_2 Compounds upon Alkali De-Intercalation. *Phys. Chem. Chem. Phys.* **2012**, *14* (44), 15571–15578.

(58) Reed, J.; Ceder, G.; Van Der Ven, A. Layered-to-Spinel Phase Transition in Li_xMnO_2. *Electrochem. Solid-State Lett.* **2002**, *4* (6), A78.

(59) Wan, C.; Nuli, Y.; Zhuang, J.; Jiang, Z. Synthesis of Spinel $LiMn_2O_4$ Using Direct Solid State Reaction. *Mater. Lett.* **2002**, *56*, 357–363.

(60) Lee, M. J.; Lee, S.; Oh, P.; Kim, Y.; Cho, J. High Performance $LiMn_2O_4$ Cathode Materials Grown with Epitaxial Layered Nanostructure for Li-Ion Batteries. *Nano Lett.* **2014**, *14* (2), 993–999.

(61) Ouyang, C. Y.; Shi, S. Q.; Lei, M. S. Jahn-Teller Distortion and Electronic Structure of $LiMn_2O_4$. *J. Alloys Compd.* **2009**, *474* (1–2), 370–374.

(62) Ishizawa, N.; Tateishi, K. Diffusion of Li Atoms in $LiMn_2O_4$ with a Disordered Spinel Structure. *J. Cermaic Soc. Japan* **2009**, *117* (1), 6–14.

(63) Hoang, K. Understanding the Electronic and Ionic Conduction and Lithium Over-Stoichiometry in $LiMn_2O_4$ spinel. *J. Mater. Chem. A* **2014**, *2* (43), 18271–18280.

(64) Yabuuchi, N.; Yano, M.; Kuze, S.; Komaba, S. Electrochemical Behavior and Structural Change of Spinel-Type $Li[Li_XMn_{2-x}]O_4$ (x = 0 and 0.2) in Sodium Cells. *Electrochim. Acta* **2012**, *82*, 296–301.

(65) Ling, C.; Mizuno, F. Phase Stability of Post-Spinel Compound AMn_2O_4 (A = Li, Na, or Mg) and Its Application as a Rechargeable Battery Cathode. *Chem. Mater.* **2013**, *25* (15), 3062–3071.

(66) Awaka, J.; Watanabe, T.; Akimoto, J.; Tokiwa, K.; Takahashi, Y.; Kijima, N.; Maruta, Y. High-Pressure Synthesis and Crystal Structure Analysis of $NaMn_2O_4$ with the Calcium Ferrite-Type Structure. *J. Solid State Chem.* **2005**, *179* (1), 169–174.

(67) Datta, M. K.; Kuruba, R.; Jampani, P. H.; Chung, S. J.; Saha, P.; Epur, R.; Kadakia, K.; Patel, P.; Gattu, B.; Manivannan, A.; et al. Electrochemical Properties of a New Nanocrystalline $NaMn_2O_4$ Cathode for Rechargeable Sodium Ion Batteries. *Mater. Sci. Eng. B Solid-State Mater. Adv. Technol.* **2014**, *188*, 1–7.

(68) Blanc, L.; Sun, X.; Nazar, L. F.; Bonnick, P.; Cabana, J.; Nolis, G. M. $NaV_{1.25}Ti_{0.75}O_4$: A Potential Post-Spinel Cathode Material for Mg Batteries . *Chem. Mater.* **2017**, *30* (1), 121–128.

(69) Sharma, N.; Shaju, K. M.; Subba Rao, G. V.; Chowdari, B. V. R. Iron-Tin Oxides with $CaFe_2O_4$ Structure as Anodes for Li-Ion Batteries. *J. Power Sources* **2003**, *124* (1), 204–212.